PHYSICAL REVIEW D **78,** 064054 (2008)

Simulating coalescing compact binaries by a new code (SACRA)

Tetsuro Yamamoto and Masaru Shibata
Graduate School of Arts and Sciences, University of Tokyo, Komaba, Meguro, Tokyo 153-8902, Japan

Keisuke Taniguchi
Department of Physics, University of Illinois at Urbana-Champaign, Illinois 61801, USA
(Received 22 May 2008; published 19 September 2008)

We report our new code, named SACRA (SimulAtor for Compact objects in Relativistic Astrophysics) for numerical relativity simulations in which an adaptive mesh refinement algorithm is implemented. In this code, the Einstein equations are solved in the Baumgarte-Shapiro-Shibata-Nakamura formalism with a fourth-order finite differencing, and the hydrodynamic equations are solved by a third-order high-resolution central scheme. The fourth-order Runge-Kutta scheme is adopted for integration in time. To test the code, simulations for coalescence of black hole-black hole, neutron star-neutron star (NS-NS), and black hole-neutron star (BH-NS) binaries are performed, and also, properties of BHs formed after the merger and gravitational waveforms are compared among those three cases. For the simulations of black hole-black hole binaries, we adopt the same initial conditions as those by Buonanno *et al.* [1] and compare numerical results. We find reasonable agreement except for a slight disagreement possibly associated with the difference in choice of gauge conditions and numerical schemes. For an NS-NS binary, we performed simulations employing both SACRA and Shibata's previous code, and find reasonable agreement between two numerical results for the final outcome and qualitative property of gravitational waveforms. We also find that the convergence is relatively slow for numerical results of NS-NS binaries, and again realize that long-term numerical simulations with several resolutions and grid settings are required for validating the results. For a BH-NS binary, we compare numerical results with our previous ones, and find that gravitational waveforms and properties of the BH formed after the merger agree well with those of our previous ones, although the disk mass formed after the merger is less than 0.1% of the total rest mass, which disagrees with the previous result. We also report numerical results of a long-term simulation (with $\sim$4 orbits) for a BH-NS binary for the first time. All these numerical results show behavior of convergence, and extrapolated numerical results for time spent in the inspiral phase agree with post-Newtonian predictions in a reasonable accuracy. These facts validate the results by SACRA.

DOI: 10.1103/PhysRevD.78.064054 PACS numbers: 04.25.D−, 04.30.−w, 04.40.Dg

I. INTRODUCTION

Coalescence of binary compact objects such as binaries of two neutron stars (NS-NS), black hole and neutron star (BH-NS), and two black holes (BH-BH) is the most promising source for kilometer-size laser-interferometric gravitational wave detectors such as LIGO, VIRGO, and LCGT. To detect gravitational waves and to analyze the gravitational wave signals for extracting physical information of the sources, it is necessary to prepare theoretical templates of gravitational waves from the coalescing compact binaries. Motivated by this fact, significant effort has been paid in the past two decades. For theoretically computing gravitational waveforms in a relatively early inspiral phase, post-Newtonian approximations are the robust approach [2]. On the other hand, for studying the last inspiral and merger phases of the coalescing binaries in which general relativistic effects are significantly strong and any approximation breaks down, numerical relativity is the unique approach.

In the past decade, in particular, in the past three years, a wide variety of general relativistic simulations have been performed for the coalescence of NS-NS binaries [3–11] and BH-BH binaries [12–28] (see also early-stage results for merger of BH-NS binaries [29–31]). Since 1999, a variety of simulations have been performed for the inspiral and merger of NS-NS binaries after the first success of Shibata and Uryū [3]. Shibata, Uryū, and Taniguchi have then performed simulations focusing mainly on the merger process and the final fate [4]. Their simulations were done for a variety of equations of state (EOS) as well as for a wide range of mass of two NSs. They have clarified that the final outcome of the merger (formation of a BH or a hypermassive neutron star; hereafter HMNS) depends strongly on the total mass of the system and on the chosen EOSs. In the latest paper [5], they clarified that with stiff EOSs such as the Akmal-Pandharipande-Ravenhall one [32], a BH is not promptly formed even for a system of the total mass $\sim 2.8 M_\odot$, but an HMNS is a likely outcome. They also indicated that the formed HMNSs have an elliptical shape because of their rapid rotation, and hence, quasiperiodic gravitational waves of frequency $\sim$3–4 kHz will be emitted for a long time (for $\sim$100 cycles) in the absence of dissipative mechanisms except for gravitational

wave emission. The integrated effective amplitude of such gravitational waves may be large enough to be detected by advanced laserinterferometric gravitational wave detectors [4,33]. In the last couple of years, long-term simulations for the inspiral of NS-NS binaries have been also done. In particular, in the latest simulations, 3–5 inspiral orbits are stably followed [8–11], and also, the computations are continued until the system settles down approximately to a stationary state even in the case that a BH is the final outcome. Preliminary simulations for merger of magnetized NSs have been also performed recently [7,9] (although it is not clear whether or not many of crucial magnetohydrodynamic instabilities are resolved in these simulations). However, in most of these works, very simple Γ-law EOSs are adopted for modeling the NSs, and hence, realistic simulations with a variety of realistic EOSs have not been done yet.

The last three years have also witnessed great progress in simulations of BH-BH binaries, starting with the first stable simulation of orbiting and merging BHs by Pretorius [12] and development of the moving puncture approach [13,14] in 2005. Since then, a large number of simulations have been done on the late inspiral and merger of BH-BH binaries [12–28]. These works have clarified that the merger waveforms are universally characterized by a quasinormal mode ringdown. They have also shown that a large kick velocity is excited at the merger in the cases that the masses of two BHs are not equal and/or the spin and orbital angular momentum vectors misalign. The latest works with a high accuracy [23–28] compare the numerical gravitational waveforms with post-Newtonian ones and assess the accuracy of the post-Newtonian waveforms [2]. In particular, the numerical simulation of Ref. [28] presents highly accurate gravitational waves, which assess the accuracy of the post-Newtonian gravitational waves with a level much beyond the previous analysis. They clarify that the so-called Taylor T4 post-Newtonian gravitational waveforms are very accurate at least up to the last two orbits before the merger for the equal-mass, nonspinning BH-BH binaries. This work shows a monumental achievement of numerical relativity because it demonstrates that numerical relativity could provide inspiral waveforms for BH-BH binaries more accurate than the post-Newtonian waveforms.

However, simulations for coalescing compact binaries have been performed only for a restricted parameter space. Because the ultimate goal is to prepare a template family that covers gravitational waveforms for almost all the possible parameters for binary compact objects, the present status is regarded as a preliminary one from the view point of gravitational wave astronomy. For example, for BH-BH binaries, the simulations have been primarily performed for the case that the spin vector of BHs aligns with the orbital angular momentum vector and the magnitude of the BH spin is not extremely large. The simulations for BH-BH binaries of unequal-mass and misaligned spin have been also performed only for the restricted cases. For NS-NS binaries, the simulations have been also primarily performed for the case that masses of two NSs are equal, and the cases of unequal-mass have been investigated in a small mass range. Moreover, the simulations have been performed adapting a few EOSs, mostly a simple Γ-law EOS. Because the EOS of NSs is still unknown, it is necessary to perform simulations choosing a wide variety of EOSs.

To perform a number of simulations for various parameters of compact objects, an efficient scheme for the numerical simulation is necessary. For the two-body problem considered here, adaptive mesh-refinement (AMR) algorithm is well suited for this purpose [34]. The reason is described as follows: In the two-body problem, there are three characteristic length scales; the radius of compact objects R, the orbital separation r, and the gravitational wave length $\lambda \approx \pi(r^3/M)^{1/2}$, where M is the total mass of the system. We have to accurately resolve these three scales. These scales obey the relation $R < r < \lambda$, and typically, $R \ll \lambda$. Thus, an issue to be resolved in this problem is to assign an appropriate resolution for each scale of significantly different magnitude. To resolve each compact object accurately, the grid spacing Δx in its vicinity has to be much smaller than R ($R/\Delta x$ should be larger than $\sim$20). On the other hand, gravitational waves have to be extracted from the geometric variables in the wave zone. This implies that the size of the computational region should be larger than λ. By simply using a uniform grid, the required grid number in one direction is $N_g = 2\lambda/\Delta x$, where the factor 2 comes from the fact that there are plus and minus directions in each axis. Because of the facts $r \gtrsim 2R$ and $R > M$, the required value of N_g is larger than several hundreds. To follow the binary inspiral from $r \sim 5R$, N_g has to be larger than 10^3. Even by supercomputers currently available for the general users, it approximately takes at least a month to perform a simulation of such a huge grid number. This implies that it is not feasible to perform a number of simulations for a wide variety of the parameters.

In the AMR algorithms, one can change the grid spacing and the grid structure arbitrarily for different scales, preserving the required grid-resolution for each scale. To accurately resolve each star in a binary, we need to take $N_g \sim 2R/\Delta x \sim 100$ to cover the region in the vicinity of the compact stars. However, for other regions, we do not have to take such a small grid spacing. In particular, we can save the grid number in the distance zone. To follow the propagation of gravitational waves in the wave zone, the required grid spacing is $\sim$0.05–0.1λ, which is larger than Δx by an order of magnitude. Thus, by choosing such a large grid spacing (and correspondingly, a large time step) in the wave zone, we can significantly save the grid number for

covering the large computational region as well as computational costs. Because of this reason, the AMR algorithms are employed by many numerical relativity groups now (e.g., [8,9,12,17]), which have provided a variety of numerical results recently.

Motivated by the facts mentioned above, we have developed a new code in which an AMR algorithm is implemented, named SACRA (SimulAtor for Compact objects in Relativistic Astrophysics) [35]. This code can evolve not only BH-BH binaries but also NS-NS and BH-NS binaries with a variety of EOSs. In SACRA, the Einstein equations are solved in a similar AMR technique to that adopted in Ref. [17]. Namely, we adopt a fourth-order finite differencing scheme for spatial derivatives and a fourth-order Runge-Kutta scheme for integration forward in time. For the AMR algorithm, six buffer zones are prepared at the refinement boundaries and for the interpolation at the refinement boundaries, fifth-order Lagrangian interpolation scheme in space and second-order Lagrangian interpolation scheme in time are adopted. For simplicity, the size and the grid spacing of computational domain for each refinement level are fixed, although the computational domain can move with the compact objects. We find that this scheme is so stable that we do not have to introduce the Kreiss-Oliger-type dissipation, which is often necessary in some AMR codes. For solving the hydrodynamic equations, we adopt a high-resolution central scheme proposed by Kurganov and Tadmor [36] with a third-order interpolation for reconstructing the fluid flux at cell interfaces. For implementing the AMR algorithm, six buffer zones are also prepared as in the gravitational field. Fifth-order and second-order Lagrangian interpolations are basically adopted in space and in time, respectively, although a limiter function is applied in the time interpolation for a region where fluid variables vary steeply. We also find that with this scheme, a stable long-term evolution is feasible for NS-NS and BH-NS binaries.

The paper is organized as follows: In Sec. II, we briefly describe the basic equations, the gauge conditions, the methods for extracting gravitational waves, and the quantities used in the analysis for the numerical results. We describe an AMR scheme, which we employ in SACRA in Sec. III. In Sec. IV, numerical results for the simulation of BH-BH, NS-NS, and BH-NS binaries are presented separately. The simulations were performed for a variety of grid resolutions and grid structures. Convergence of numerical results shows validity of our code. Section V is devoted to a summary. Throughout this paper, we adopt the geometrical units in which $G = c = 1$, where G and c are the gravitational constant and the speed of light. Latin and Greek indices denote spatial components (x, y, z) and spacetime components (t, x, y, z), respectively: $r \equiv \sqrt{x^2 + y^2 + z^2}$. $\delta_{ij} (= \delta^{ij})$ denotes the Kronecker delta.

II. FORMULATION

A. Brief review of basic equations

The fundamental variables for geometry in 3 + 1 decomposition are α: the lapse function, β^k: the shift vector, γ_{ij}: the metric in a three-dimensional spatial hypersurface, and K_{ij}: the extrinsic curvature. We solve the Einstein evolution equations using a slightly modified version of the BSSN (Baumgarte-Shapiro-Shibata-Nakamura) formalism [37]. In the original version of the BSSN formalism, one chooses the variables to be evolved as

$$\tilde{\gamma}_{ij} = e^{-4\phi}\gamma_{ij}, \tag{1}$$

$$\tilde{A}_{ij} = e^{-4\phi}(K_{ij} - \tfrac{1}{3}\gamma_{ij}K), \tag{2}$$

$$\phi = \tfrac{1}{12}\ln[\mathrm{tr}(\gamma_{ij})], \tag{3}$$

$$K = K_k{}^k, \tag{4}$$

$$F_i = \delta^{jk}\partial_j\tilde{\gamma}_{ik} \quad \text{or} \quad \tilde{\Gamma}^i = -\tilde{\gamma}^{ij}{}_{,j}. \tag{5}$$

Note that the condition $\det(\tilde{\gamma}_{ij}) = 1$ has to be satisfied (we assume to use Cartesian coordinates). In the present approach, we also evolve $\tilde{\gamma}_{ij}$, $\tilde{A}_{ij}$, K, and F_i or $\tilde{\Gamma}^i$, whereas instead of ϕ, we evolve $W \equiv e^{-2\phi}$ following Ref. [27]. The primary reason is that we adopt the grid-center-grid in numerical simulation; when center of a BH is located approximately at a grid point, ϕ becomes too large to compute accurately. With the choice of W, such pathology can be avoided, as first pointed out by Campanelli *et al.* [13]. In this formalism, the Ricci tensor with respect to γ_{ij} is written as

$$R_{ij} = \tilde{R}_{ij} + R^W_{ij}, \tag{6}$$

where $\tilde{R}_{ij}$ is the Ricci tensor with respect to $\tilde{\gamma}_{ij}$ and

$$R^W_{ij} = \frac{1}{W}\tilde{D}_i\tilde{D}_jW + \tilde{\gamma}_{ij}\left(\frac{1}{W}\tilde{D}_k\tilde{D}^kW - \frac{2}{W^2}\tilde{D}_kW\tilde{D}^kW\right). \tag{7}$$

Here, $\tilde{D}_i$ is the covariant derivative with respect to $\tilde{\gamma}_{ij}$. Merits of using W instead of $\chi = e^{-4\phi}$ proposed in Ref. [13] are that (i) the equation for R^W_{ij} is slightly simplified and (ii) even for $W \to 0$, no singular term appears in the basic equation in which R^W_{ij} always appears in the form of $W^2R^W_{ij}$.

In SACRA, we implement both equations for F_i and $\tilde{\Gamma}^i$. As we show in Sec. IV, numerical results do not depend strongly on the choice of the variables.

For the condition of the lapse function α and the shift vector β^i, we adopt dynamical gauge conditions. For the case that we adopt the Shibata-Nakamura-type BSSN formalism (hereafter F_i-BSSN formalism), the gauge equations adopted are [29]

$$(\partial_t - \beta^i \partial_i)\alpha = -2\alpha K, \tag{8}$$

$$\partial_t \beta^i = 0.75\tilde{\gamma}^{ij}(F_j + \Delta t \partial_t F_j). \tag{9}$$

Here, Δt denotes a time step in numerical simulation and the second term on the right-hand side of Eq. (9) is introduced for stabilization of numerical computation. For the Baumgarte-Shapiro-type BSSN formalism (hereafter the $\tilde{\Gamma}^i$-BSSN formalism), we also employ Eq. (8) for evolution of α, whereas for β^k, we adopt the so-called Γ-freezing gauge [38]

$$(\partial_t - \beta^j \partial_j)\beta^i = 0.75B^i, \tag{10}$$

$$(\partial_t - \beta^j \partial_j)B^i = (\partial_t - \beta^j \partial_j)\tilde{\Gamma}^i - \eta_s B^i, \tag{11}$$

where B^i is an auxiliary variable, and η_s is an arbitrary constant. In the present work, we basically choose $\eta_s \approx 1/m$ for BH-BH and BH-NS binaries, and $\approx 3/m$ for NS-NS binaries. Here, m denotes the irreducible mass for a BH and mass in the case of isolation for an NS. As shown in Ref. [17], the coordinate radius of the apparent horizon is larger for larger value of η_s. This implies that the region near the BH is not well resolved for too small values of η_s, whereas for too large values of η_s, the BH is not covered only by the finest level in the AMR algorithm. For $\eta_s = 1/m$ and $2/m$, the coordinate radius of the apparent horizon of a nonspinning BH is $\sim 0.8m$ and $1.1m$, respectively.

The adopted spatial gauge condition is different for numerical simulations with the F_i-BSSN and $\tilde{\Gamma}^i$-BSSN formalisms. Difference in numerical results computed by both formalisms results primarily from this difference.

During evolution, we enforce the following constraints on $\tilde{\gamma}_{ij}$ and $\tilde{A}_{ij}$ at every time step

$$\det(\tilde{\gamma}_{ij}) = 1, \tag{12}$$

$$\mathrm{Tr}\,(\tilde{A}_{ij}) = 0. \tag{13}$$

The reason for this is that these constraints are violated slightly due to numerical error. Specifically, we reset, after every time evolution, as

$$\tilde{\gamma}_{ij} \to [\det(\tilde{\gamma}_{ij})]^{-1/3}\tilde{\gamma}_{ij}, \tag{14}$$

$$\tilde{A}_{ij} \to [\det(\tilde{\gamma}_{ij})]^{-1/3}\tilde{A}_{ij} - \tfrac{1}{3}\tilde{\gamma}_{ij}\,\mathrm{Tr}(\tilde{A}_{ij}), \tag{15}$$

$$W \to [\det(\tilde{\gamma}_{ij})]^{-1/6}W, \tag{16}$$

$$K \to K + \mathrm{Tr}(\tilde{A}_{ij}). \tag{17}$$

We note that in this adjustment, γ_{ij} and K_{ij} are unchanged.

We do not add any constraint-violation damping terms in SACRA. We monitor violation of Hamiltonian and momentum constraints computing L2 norm for them, and find that their growth time scales are much longer than the dynamical time scale even in the absence of the damping terms. (Note that an exception is at the formation of BH after the merger of NS-NS binaries, at which the degree of constraint violation increases rapidly by an order of magnitude.)

The fundamental variables for the hydrodynamics are ρ: the rest-mass density ε: the specific internal energy P: the pressure u^μ: the four velocity and the three velocity defined by

$$v^i = \frac{dx^i}{dt} = \frac{u^i}{u^t}. \tag{18}$$

For our numerical implementation of the hydrodynamic equations, we define a weighted density, a weighted four velocity, and a specific energy defined, respectively, by

$$\rho_* \equiv \rho\alpha u^t W^{-3}, \tag{19}$$

$$\hat{u}_i \equiv h u_i, \tag{20}$$

$$\hat{e} \equiv h\alpha u^t - \frac{P}{\rho\alpha u^t}, \tag{21}$$

where $h = 1 + \varepsilon + P/\rho$ denotes the specific enthalpy. The general relativistic hydrodynamic equations are written into a conservative form for variables ρ_*, $\rho_*\hat{u}_i$, and $\rho_*\hat{e}$. Then, we solve these equations using a high-resolution central scheme [36,39]. In our approach, the transport terms such as $\partial_i(\cdots)$ are computed by the scheme of Kurganov-Tadmor [36] with a third-order (piecewise parabolic) spatial interpolation for reconstructing numerical fluxes.

In the present work, the initial condition for NSs is computed with the polytropic EOS

$$P = \kappa\rho^\Gamma, \tag{22}$$

where κ and Γ are the polytropic constant and the adiabatic index. Because κ is arbitrarily chosen, we set $\kappa = 1$ in the following. Γ is set to be 2 for comparing numerical results with previous ones [4,30]. During the numerical simulation, we adopt the Γ-law EOS

$$P = (\Gamma - 1)\rho\varepsilon. \tag{23}$$

Again, we set $\Gamma = 2$. Note that we have already implemented a number of EOSs in our code (e.g., [4,11]). In the future, we will perform numerical simulations in such EOSs.

At each time step, $w = \alpha u^t$ is determined by solving an algebraic equation derived from the normalization relation $u^\mu u_\mu = -1$ and EOS. Specifically, the equation is written as

$$w^2 = 1 + \frac{\gamma^{ij}\hat{u}_i\hat{u}_j}{h^2}, \tag{24}$$

where in the chosen EOS, h is written as

$$h = [\hat{e}w\Gamma - (\Gamma - 1)][w^2\Gamma - (\Gamma - 1)]^{-1}. \tag{25}$$

After w and h are determined, the primitive variables such as ρ, ε, and u_i are updated as $\rho = \rho_* W^3/w$, $\varepsilon = (h - 1)/\Gamma$, and $u_i = \hat{u}_i/h$.

Because any conservation scheme of hydrodynamics is unable to evolve a vacuum, we have to introduce an artificial atmosphere outside NSs. Density of the atmosphere should be as small as possible, to avoid spurious effect due to it. In the present case, we initially assign a small rest-mass density in vacuum as

$$\rho = \begin{cases} \rho_{\rm at} & r \le r_0, \\ \rho_{\rm at} e^{1-r/r_0} & r > r_0, \end{cases} \tag{26}$$

where we choose $\rho_{\rm at} = \rho_{\rm max} \times 10^{-8}$ for NS-NS binaries and 10^{-9} for BH-NS binaries. Here, $\rho_{\rm max}$ is the maximum rest-mass density of the NS. r_0 is a coordinate radius of $\sim$10–20M, where M is the ADM (Arnowitt-Deser-Misner) mass of the system. With such a choice of parameters, the total amount of the rest mass of the atmosphere is about 10^{-5} of the rest mass of the NS. Thus, spurious effects due to the presence of the atmosphere, such as accretion of the atmosphere onto NS and BH, the resulting dragging effect against orbital motion, gravitational effect by the atmosphere, and formation of a disk around the final outcomes, play a negligible role in the present context.

In the presence of a BH, location of apparent horizon is determined by an apparent horizon finder. In our method, we derive a two-dimensional elliptic-type equation for the radius of the apparent horizon and iteratively solve this equation until a sufficient convergence is achieved. This method is essentially the same as that in Ref. [40], but in SACRA, we implement a simpler scheme for computing the source term for the elliptic-type equation. We briefly describe this method in Appendix A.

B. Formulation for extracting gravitational waves

Gravitational waves are extracted computing the outgoing component of the Newman-Penrose quantity (the so-called Ψ_4), which is defined by

$$\Psi_4 = -{}^{(4)}R_{\alpha\beta\gamma\delta} n^\alpha \bar{m}^\beta n^\gamma \bar{m}^\delta, \tag{27}$$

where ${}^{(4)}R_{\alpha\beta\gamma\delta}$ is Riemann tensor with respect to spacetime metric $g_{\mu\nu}$, and n^α and $\bar{m}^\beta$ are parts of null tetrad $(n^\alpha, \ell^\alpha, m^\alpha, \bar{m}^\alpha)$. Specifically, n^α and ℓ^α are outgoing and ingoing null vectors, whereas m^α is a complex null vector orthogonal to n^α and ℓ^α. The null tetrad satisfies the conditions

$$-n^\alpha \ell_\alpha = 1 = m^\alpha \bar{m}_\alpha, \tag{28}$$

and $g_{\mu\nu}$ is written as

$$g_{\mu\nu} = -n_\mu \ell_\nu - n_\nu \ell_\mu + m_\mu \bar{m}_\nu + m_\nu \bar{m}_\mu. \tag{29}$$

Denoting n^μ by $n^\mu = (N^\mu - r^\mu)/\sqrt{2}$, where N^μ is unit timelike hypersurface normal $(\alpha^{-1}, -\beta^i \alpha^{-1})$ and r^μ is a unit radial vector orthogonal to N^μ and m^μ, Ψ_4 is rewritten to

$$\Psi_4 = -\frac{1}{2}[{}^{(4)}R_{\alpha\beta\gamma\delta} N^\alpha \bar{m}^\beta N^\gamma \bar{m}^\delta - 2{}^{(4)}R_{\alpha\beta\gamma\delta} N^\alpha \bar{m}^\beta r^\gamma \bar{m}^\delta + {}^{(4)}R_{\alpha\beta\gamma\delta} r^\alpha \bar{m}^\beta r^\gamma \bar{m}^\delta]. \tag{30}$$

Using the following relations,

$${}^{(4)}R_{\alpha i\gamma j} N^\alpha N^\gamma = R_{ij} - K_{ik} K_j{}^k + K K_{ij} \equiv \mathcal{E}_{ij}, \tag{31}$$

$${}^{(4)}R_{\alpha ijk} N^\alpha = D_j K_{ik} - D_k K_{ij} \equiv \mathcal{B}_{ijk}, \tag{32}$$

$${}^{(4)}R_{ijkl} = R_{ijkl} + K_{ik} K_{jl} - K_{il} K_{jk} \equiv \mathcal{R}_{ijkl}, \tag{33}$$

where D_i, R_{ij}, and R_{ijkl} are covariant derivative, Ricci tensor, and Riemann tensor with respect to three-metric γ_{ij}. Thus, Ψ_4 is written only by geometric variables in 3 + 1 formalism. Note that for deriving Eq. (31), we assume that Ψ_4 is extracted in a vacuum region. In addition, we have the following identity in three-dimensional space because of symmetric and antisymmetric relations for $\mathcal{R}_{ijkl}$:

$$\mathcal{R}_{ijkl} = \gamma_{ik}\mathcal{R}_{jl} - \gamma_{il}\mathcal{R}_{jk} - \gamma_{jk}\mathcal{R}_{il} + \gamma_{jl}\mathcal{R}_{ik} - \frac{1}{2}\mathcal{R}(\gamma_{ik}\gamma_{jl} - \gamma_{il}\gamma_{jk}), \tag{34}$$

where $\mathcal{R}_{ik} = \mathcal{R}_{ijk}{}^j$ and $\mathcal{R} = \mathcal{R}_k{}^k$. Then, we find

$$\mathcal{E}_{ij} \bar{m}^i \bar{m}^j = \mathcal{R}_{ijkl} r^i \bar{m}^j r^k \bar{m}^l, \tag{35}$$

and obtain a simple formula

$$\Psi_4 = -(\mathcal{E}_{ij} \bar{m}^i \bar{m}^j - \mathcal{B}_{ijk} \bar{m}^i r^j \bar{m}^k). \tag{36}$$

For $r \to \infty$, Ψ_4 is written as

$$\Psi_4 = -\tfrac{1}{2}(\ddot{h}_+ - i\ddot{h}_\times), \tag{37}$$

where h_+ and $h_\times$ are + and × modes of gravitational waves, respectively. Thus, by performing time integration of $2\Psi_4$ twice (and by appropriately choosing integration constants), one can derive gravitational waveforms. More specifically, we decompose Ψ_4 into tensor spherical harmonic modes of (l, m) by surface integral at a sufficiently large radius as usually done (e.g., see Ref. [17] in detail), and pay particular attention to harmonics of low quantum numbers. In this paper, we compute the modes with $2 \le l \le 4$.

From Ψ_4, energy, linear momentum, and angular momentum dissipation rates by gravitational waves are computed by

$$\frac{dE}{dt} = \lim_{r\to\infty}\left[\frac{r^2}{16\pi} \oint_S dA \left| \int \Psi_4 dt \right|^2\right], \tag{38}$$

$$\frac{dP_i}{dt} = \lim_{r\to\infty}\left[\frac{r^2}{16\pi} \oint_S dA \frac{x^i}{r} \left| \int \Psi_4 dt \right|^2\right], \tag{39}$$

$$\frac{dJ_z}{dt} = \lim_{r\to\infty}\left[\frac{r^2}{16\pi}\mathrm{Re}\left\{\oint_S dA\left(\int \partial_\varphi \Psi_4 dt\right)\times\left(\iint \bar{\Psi}_4 dt dt'\right)\right\}\right], \quad (40)$$

where $\oint dA = \oint d(\cos\theta)d\varphi$ denotes an integral on two surface of a constant coordinate radius and $\bar{\Psi}_4$ is the complex conjugate of Ψ_4. In the actual simulation, gravitational waves are extracted at finite radii, and then, by an extrapolation, asymptotic gravitational waveforms should be derived. In such a procedure, we estimate the dissipation rates by exchanging r to a proper radius approximately defined by $D = r(1 + m_0/2r)^2$, where r is the coordinate radius, D approximately denotes the proper radius, and m_0 is sum of mass of two compact objects [see Eq. (46)].

C. Diagnostics

1. Mass, linear momenta, and angular momenta

We monitor the ADM mass M, the linear momenta P_i, and the angular momenta J_i during the evolution. To do so, we define integrals on two surface of a coordinate radius r

$$M_{\mathrm{ADM}}(r) = \frac{1}{16\pi}\oint_r \sqrt{\gamma}\gamma^{ij}\gamma^{kl}(\gamma_{ik,j} - \gamma_{ij,k})dS_l, \quad (41)$$

$$P_i(r) = \frac{1}{8\pi}\oint_r \sqrt{\gamma}(K_i{}^j - K\gamma_i{}^j)dS_j, \quad (42)$$

$$J_i(r) = \frac{1}{8\pi}\epsilon_{ilk}\oint_r \sqrt{\gamma}x^l(K^{jk} - K\gamma^{jk})dS_j. \quad (43)$$

Then, we extrapolate these quantities for $r \to \infty$ to obtain the ADM mass M, the linear momenta P_i, and the angular momenta J_i. Throughout this paper, the initial values of M_{ADM} and J_z are denoted by M_0 and J_0, respectively.

When simulating a spacetime with NSs, we also monitor the total baryon rest mass (M_*)

$$M_* = \int \rho u^t \sqrt{-g}d^3x. \quad (44)$$

In the simulation with a unigrid domain, it is easy to guarantee that M_* is conserved by adopting standard schemes of numerical hydrodynamics (except for a possible slight error associated with an artificial treatment of atmosphere). In the schemes in which an AMR algorithm is implemented, it is not straightforward to guarantee that M_* is conserved when regridding is carried out. In our present scheme, M_* is not strictly conserved, and it is necessary to confirm that the violation of the conservation is within an acceptable level.

2. Spin and mass of the formed BH

For BH-BH and BH-NS binaries, apparent horizons are determined during the evolution, and thus, we monitor their area. From the area, the irreducible mass of each BH is defined by

$$m_i = \sqrt{\frac{A_{\mathrm{AH},i}}{16\pi}}, \quad (45)$$

where $A_{\mathrm{AH},i}$ is the area of each BH. For BH-BH binaries, we define a total mass at $t = 0$ as

$$m_0 = m_1 + m_2, \quad (46)$$

and present all the numerical results in units of m_0. (In this paper, $m_0 = 2m_1$ because we only consider the equal-mass BH-BH binaries.)

After the merger of compact binary objects, a rotating BH is often formed in the end. To determine properties of the formed BH, we analyze several quantities of the apparent horizon of such BH. Specifically, we compute the area A_{AH}, polar circumferential length C_p, and equatorial circumferential length C_e, of the apparent horizon. If the formed BH is a Kerr BH and the system relaxes to a stationary state, the area obeys the relation of

$$A_{\mathrm{AH}} = 8\pi M_{\mathrm{BHf}}^2(1 + \sqrt{1 - a^2}), \quad (47)$$

where M_{BHf} and a are mass and spin parameter of the Kerr BH, respectively. Also, C_e should be $4\pi M_{\mathrm{BHf}}$ and C_p/C_e is a known function composed only of a as

$$\frac{C_p}{C_e} = \frac{\sqrt{2\hat{r}_+}}{\pi}E(a^2/2\hat{r}_+), \quad (48)$$

where $\hat{r}_+ = 1 + \sqrt{1 - a^2}$ and $E(z)$ is an elliptic integral defined by

$$E(z) = \int_0^{\pi/2}\sqrt{1 - z\sin^2\theta}d\theta. \quad (49)$$

In the analysis of numerical results, we determine the spin parameter a, from Eq. (48) providing C_p/C_e by direct measurement from numerical results. Then, M_{BHf} can be determined either from Eq. (47) or from $C_e/4\pi$. We calculate the BH mass using both methods and check that two results agree well. In addition, we can infer the final ADM mass of the system from the initial value of the ADM mass and the total radiated energy by gravitational waves, and the final angular momentum of the system from the initial angular momentum and the total radiated one. These values have to also agree with the mass and angular momentum of a system finally formed, due to the presence of conservation laws.

3. Gravitational waves

We compare inspiral orbital trajectories with the results by the so-called Taylor T4 post-Newtonian formula for two point masses in quasicircular orbits (see, e.g., Refs. [23,28] for a detailed description of various post-Newtonian formulas). Recent high-accuracy simulations for equal-mass (nonspinning or corotating) BH-BH binaries have proven

that the Taylor T4 formula provides their orbital evolution and gravitational waveforms with a high accuracy at least up to about one orbit before the merger. In this formula, the angular velocity Ω is determined by solving [23]

$$\frac{dX}{dt} = \frac{64\eta X^5}{5M_0}\Bigg[1 - \frac{743 + 924\eta}{336}X + \left(4\pi - \frac{47}{3}\chi\right)X^{3/2} + \left(\frac{34\,103}{18\,144} + \frac{13\,661\eta}{2016} + \frac{59\eta^2}{18}\right)X^2 - \Bigg\{\frac{4159 + 15\,876\eta}{672}\pi + \left(\frac{31\,811}{1008} - \frac{5039}{84}\eta\right)\chi\Bigg\}X^{5/2} + \Bigg\{\frac{16\,447\,322\,263}{139\,708\,800} - \frac{1712\gamma_E}{105} + \frac{16\pi^2}{3} + \left(\frac{-56\,198\,689}{217\,728} + \frac{451}{48}\pi^2\right)\eta + \frac{541}{896}\eta^2 - \frac{5605}{2592}\eta^3 - \frac{856}{105}\log(16X)\Bigg\}X^3 + \left(\frac{-4415}{4032} + \frac{358\,675}{6048}\eta + \frac{91\,495}{1512}\eta^2\right)\pi X^{7/2}\Bigg], \tag{50}$$

where $X = [m_0\Omega(t)]^{2/3}$ is a function of time, η is a ratio of the reduced mass to the total mass m_0, $\gamma_E = 0.577\cdots$ is the Euler constant, and $\chi \equiv S/4m_0^2$, which is defined from the sum of spin angular momentum of BHs S. The spin is present for each BH of BH-BH binaries considered in this paper. In Eq. (50), we omit to write terms associated with the difference in spins, because we only consider the case that the spins of two BHs are equal.

From $X(t)$, gravitational waveforms are determined from

$$h_+(t) = \frac{4\eta m_0 X}{D}A(X)\cos[\Phi(t) + \delta], \tag{51}$$

$$h_\times(t) = \frac{4\eta m_0 X}{D}A(X)\sin[\Phi(t) + \delta], \tag{52}$$

where $A(X)$ is a nondimensional function of X for which $A(X) \to 1$ for $X \to 0$, δ is an arbitrary phase, and

$$\Phi(t) = 2\int \Omega(t)dt. \tag{53}$$

For $A(X)$, we adopt the 2.5 post-Newtonian formula (e.g., Ref. [28]).

III. ADAPTIVE MESH REFINEMENT

A. Adaptive mesh refinement for the Einstein equations

Our AMR algorithm for solving the Einstein evolution equations are very similar to that described in Ref. [17]: We employ the Berger-Oliger-type AMR algorithm [34] with the centered fourth-order finite-differencing in space for evaluating spatial derivatives and with the lop-sided fourth-order finite differencing for advection terms like $\beta^i\partial_i W$. For integration forward in time, the fourth-order Runge-Kutta scheme is adopted. There are also slight differences between our scheme and the scheme of Ref. [17]. The main difference comes from the choice of grid structure; we adopt the grid-center-grid, whereas the code of Ref. [17] adopts the cell-center-scheme. The reason for our choice is simply that we felt that with the grid-center-grid, it is easier to implement the interpolation and extrapolation required to be carried out at refinement boundaries in any AMR algorithm. Because of the difference in the grid structure, our interpolation and extrapolation schemes around the refinement boundaries are different from those of Ref. [17]. In order to clarify the difference, we describe our method in detail in the following.

As in the code of Ref. [17], the entire numerical domain is composed of a hierarchy of nested Cartesian grids. The hierarchy consists of L levels of refinement domains of indices $l = 0, 1, \cdots, L-1$. Here, $l = 0$ is the coarsest level, whereas $l = L-1$ is the finest one. Each refinement level consists of one or two domains. For coarser levels of $l \le L_1$, where $L_1 (< L-1)$ is a constant, the number of the refinement domain is one, and their grid locations are fixed throughout numerical simulation. We call this type of domain the coarser domain in the following. On the other hand, for finer levels with $l > L_1$, the number of the refinement domain is two, each of which covers a region near the center of two compact objects. We call this type of domain the finer domain. For the levels composed of only one domain, we initially choose the grid for which the center agrees (approximately) with mass center of the system. For the levels composed of two domains, the grid center is chosen to agree approximately with the center of the compact objects at $t = 0$.

Each domain is in general composed of $(2N+1)\times(2N+1)\times(2N+1)$ grid points for the x-y-z axis directions, where N is an even integer, and it is the same value for all the domains. Note that in counting the grid number, the number of buffer zone (see below) is not included. When symmetries are imposed, the grid number is appropriately saved. For example, when the equatorial-plane symmetry is imposed, the grid number is $(2N+1)\times(2N+1)\times(N+1)$ for the x-y-z axis directions. The grid spacing in each level is fixed to be uniform and denoted by h_l for the l-th level. For simplicity, a refinement of factor 2 is adopted, i.e., $h_l = h_0/2^l$, where h_0 is the largest grid spacing. Thus, the length of a side of each cube is $2Nh_l$ for the l-th level.

Specifically, the center of any finer domain is arranged to agree approximately with mass center of a compact object. To guarantee this arrangement during time evolution, regridding is necessary as the compact objects move. Following Ref. [17], we use the shift to track the position of BH centers by integrating

$$\partial_t x^i_{\rm BH} = -\beta^i(x^j_{\rm BH}), \tag{54}$$

where $x^i_{\rm BH}$ denotes the center of a BH. The shift vector at $x^i_{\rm BH}$ is determined by the linear interpolation of β^i in the finest refinement levels. The time integration of Eq. (54) is performed with the fourth-order Runge-Kutta scheme. For the case of NSs, coordinate position of the center, $x^i_{\rm NS}$ is determined by searching for the local maximum density at every time step. Here, the maximum density implies the maximum of ρ_* (not ρ) in SACRA.

During time evolution, the finer domains are moved for the i-th axis direction, whenever the following condition is satisfied:

$$|x^i_{\rm BH} - x^i_{l0}| \geq 2h_l \quad \text{for BHs,} \tag{55}$$

$$|x^i_{\rm NS} - x^i_{l0}| \geq 2h_l \quad \text{for NSs,} \tag{56}$$

where x^i_{l0} denotes the center of a finer domain in the l-th level. Then, we translate the finer domain by $2h_l$ toward the x^i axis direction. Here, the factor 2 comes from the requirement that a refinement boundary surface of a domain of level l (hereafter, referred to as ''child domain'') always overlaps with a surface of a domain of level $l-1$ (hereafter ''parent domain''), which is defined by $x^i = {\rm const}$ in the parent domain.

We arrange that each child domain of level l (≥ 1) is guaranteed to be completely covered by its parent domain of level $l-1$. Here, we determine that each child has only one parent. If there are two domains in the same level, say $(l-1)$-th level, we refer to one of two as the parent and to the other as the uncle. For more specific description, let us denote the location of grid points for the child and the parent, respectively, by (i_c, j_c, k_c) and (i_p, j_p, k_p) for (x, y, z), where i_c, j_c, k_c, i_p, j_p, and k_p are all in the range between $-N$ and N. We arrange that refinement boundary surfaces of the child domain, i.e., $i_c = -N$, $i_c = N$, $j_c = -N$, $j_c = N$, $k_c = -N$, and $k_c = N$ always overlap with surfaces of $x^i = {\rm const}$ in the parent domain (here, x^i denotes x or y or z). Namely, the surfaces of $i_c = -N$ and $i_c = N$ overlap with the parent's surfaces of $i = i_{p1} = {\rm const}$ and $i = i_{p2} = {\rm const}$, respectively. (This is also the case for $j_c = \pm N$ and $k_c = \pm N$.) Typically, the following conditions are satisfied: $i_{p1} \approx -N/2$ and $i_{p2} \approx N/2$. By this arrangement, our refinement procedure becomes very simple: Assigning finer quantities of the child level to its one-coarser level is straightforward because the grid points of the parent domain for $i_{p1} \leq i \leq i_{p2}$ overlap with those of the child domain.

A parent domain overlap not only with its child domain (level l) but also may overlap with another domain of level l (we call this nephew). We have to copy values of the nephew to the parent in the same procedure as described above (from the viewpoint of the child, values of the child are copied to its uncle). To carry out this procedure, we have to check status of overlapping for all the levels composed of two domains at each time step. We note that copying the finer quantities to the coarser ones is carried out at each time step that the quantities of the coarser levels are defined. [Note that the time step of the child domain is always half of that of the parent domain; cf. Equation (58).]

To evolve quantities near the refinement boundaries of a child domain, we have to prepare buffer zones and to assign an approximate value on them. Following Ref. [17], we prepare six buffer zone points along each axis (e.g., for the x axis direction, extra regions of $-N-6 \leq i \leq -N-1$ and $N+1 \leq i \leq N+6$ are prepared as the buffer zones). The quantities at the buffer zones are provided from the corresponding parent domain by the following procedure: (i) If a buffer-zone's grid point of the child domain overlaps with its parent's grid point, we simply copy the value, and (ii) if a buffer-zone's grid point of the child domain is located between its parent's grid points, the fifth-order centered Lagrangian interpolation is applied using nearby six parent's grid points. Actual three-dimensional procedure is carried out by successive one-dimensional procedures.

The interpolation procedure from the parent to the child for the child's buffer zone, which is described above, is carried out in the straightforward manner whenever the time-step level coincides between two levels. However, it does not, in general, coincide because the time step of the parent level Δt_{l-1} is twice larger than that of the child level Δt_l in typical AMR algorithms [34]. Specifically, the time-step level does not agree (i) at a child's time step of odd number, and (ii) at each Runge-Kutta sub time step. For the interpolation at such time step, we employ the following method: (I) For the inner three buffer-zone's points (e.g., $-N-3 \leq i \leq -N-1$ and $N+1 \leq i \leq N+3$ for the x axis direction), we evolve all the quantities using the fourth-order finite-differencing scheme. Because there are sufficient number of buffer-zone's points to solve the evolution equations in the inner three buffer-zone's points, no interpolation is necessary; (II) For the fourth buffer-zone's point (e.g., $i = \pm(N+4)$ for the x axis direction), all the quantities are evolved using the second-order finite-differencing scheme with no interpolation: (III) For the outer two buffer-zone's points (e.g., $-N-6 \leq i \leq -N-5$ and $N+5 \leq i \leq N+6$ for the x axis direction), the second-order Lagrangian interpolation of the parent's quantities in time is carried out to determine the values of the parent level at the corresponding child's time-step level as a first step, and then, the fifth-order Lagrangian interpolation in space is carried out.

Because there are two domains in the finer levels, they often overlap with each other. In such a case, the values of all the quantities should agree with each other. However, the evolution equations for those two domains are solved independently, and consequently, the values do not always agree. To guarantee that they agree, we simply take aver-

age of two values as $Q_1 \to (Q_1 + Q_2)/2$ and $Q_2 \to (Q_1 + Q_2)/2$, where Q_1 and Q_2 denote the values of two domains of the same refinement level. When a buffer-zone's point of one of the two domains overlaps with a point in the main region of the other domain, the values at the point of the main region are copied to those at the buffer-zone's point. When two buffer zones overlap at some points, the simple averaging, described above, is again used.

At the outer boundaries of the coarsest refinement level, an outgoing boundary condition is imposed for all the geometric variables. The outgoing boundary condition is the same as that suggested by Shibata and Nakamura [37].

It is possible to add artificial dissipation terms. Following Ref. [17], we tried to add the sixth-order Kreiss-Oliger-type dissipation term as

$$Q_l \to Q_l - \sigma h_l^6 Q_l^{(6)}, \tag{57}$$

where Q_l is a quantity in the l-th level, $Q_l^{(6)}$ is the sum of the sixth derivative along the x, y, and z axis directions, and σ is a constant of order 0.1. We performed simulations for BH-BH binaries with $\sigma = 0$ and 0.1, and found that the simulations proceed with no instability even for $\sigma = 0$ and that the numerical results depended very weakly on the dissipation. The numerical dissipation, however, spuriously accelerated the merger process for the nonzero value of σ, and as a result, the merger time was shortened slightly. Thus, in this paper, we do not add any dissipation term in the simulation. Even in hydrodynamic simulations, we do not have to add it.

Numerical simulations for BH-BH binaries reported in this paper are performed with nine or ten refinement levels, which include five or six coarser levels composed of one domain and four finer levels composed of two domains. Simulations for NS-NS binaries are performed with seven or eight refinement levels, i.e., three or four coarser levels composed of one domain and four or five finer levels composed of two domains. For BH-NS binaries, simulations are done with eight refinement levels, i.e., four coarser levels composed of one domain and four finer levels composed of two domains.

Time step for each refinement level dt_l is determined by the following rule:

$$dt_l = \begin{cases} h_{l_c}/2 & \text{for } 0 \le l \le l_c \\ h_l/2 & \text{for } l_c < l \le L - 1, \end{cases} \tag{58}$$

where $l_c = 4$ for simulations of BH-BH binary and $l_c = 2$ for NS-NS and BH-NS binaries. Namely, the Courant number is $1/2$ for the finer refinement levels with $l \ge l_c$, whereas for the coarser levels, it is smaller than $1/2$. The reason why the small Courant number is chosen for the small values of l is that with a high Courant number such as $1/2$, the numerical instability occurs near the outer boundaries for the coarsest refinement level.

B. Adaptive mesh refinement for the hydrodynamic equations

When a hydrodynamic simulation is performed employing an AMR algorithm, first of all, we have to determine for which variables the interpolation from coarser to finer levels and the copy from finer to coarser levels are carried out. In the present work, we choose ρ_*, $\hat{u}_i$, and h for the interpolation and copying procedures. The copying procedure is totally the same as that for geometric variables (see Sec. III A). The interpolation procedure is basically the same as that for geometric variables; if grid points of the child and parent domains overlap, we simply copy the values of the parent to the child, whereas if they do not overlap, we adopt the fifth-order Lagrangian interpolation. However, for the fluid variables such as ρ_* and h, this interpolation scheme could fail, in particular, in the vicinity of surface of NSs for which ρ_* is small and steeply varies. The reason for this possible failure is that the interpolation may give a negative value of ρ_* (and also $h - 1$), which is unphysical. Thus, in the case that $\rho_* < \rho_{\rm min}$ or $h < 1$ are results of the fifth-order interpolation, we adopt the first-order scheme for the interpolation (i.e., linear interpolation). Here, $\rho_{\rm min}$ is chosen to be $\rho_{\rm max}/10^8$ for NS-NS binaries and $\rho_{\rm max}/10^9$ for BH-NS binaries in the present case, where $\rho_{\rm max}$ is the initial maximum value of ρ_*. We have found that the linear interpolation is too dissipative to adopt for the entire interpolation. Therefore, this is used only in case.

We also modify the scheme of interpolation in time, which is necessary for the interpolation procedure in the buffer zone (see Sec. III A). For geometric variables, we always use the second-order interpolation scheme as described in Sec. III A. Specifically, we determine an interpolated value at a child's time step from values at three time levels of its parent, say, $n - 1$, n, and $n + 1$. Here, the interpolation is necessary for determining the values at a time t that satisfies $t^n < t < t^{n+1}$. For the fluid variables, we basically adopt the same interpolation scheme as that for the geometrical variables. However, for maintaining numerical stability, we modify it when the following relation holds:

$$(Q^{n+1} - Q^n)(Q^n - Q^{n-1}) < 0. \tag{59}$$

Here, Q is ρ_* or $\hat{u}_i$ or h, and Q^n denotes Q at t^n. In this case, we adopt the first-order interpolation scheme, only using Q^{n+1} and Q^n. Namely, a limiter procedure is introduced. We have found that this prescription is robust for stabilizing numerical computation.

After the interpolation or the copy is carried out, we have to determine values of primitive variables such as ρ, u^t, and ε. In the present choice of the variables to be interpolated or copied (ρ_*, $\hat{u}_i$, and h), this procedure is quite simple. From h and $\hat{u}_i$, w is determined from Eq. (24). Then, ρ is computed by $\rho_* W^3/w$. Because the relation $h = 1 + \Gamma\varepsilon$ holds, ε is also immediately obtained.

Even if we adopt more complicated EOSs, ρ and w are immediately calculated. In general EOSs, h is a complicated function of ρ and ε. Thus, the procedure for getting ε may be much more complicated. However, ρ is obtained very easily, and hence, ε should be obtained by simply solving a one-dimensional equation for $h = h(\varepsilon)$.

C. Extracting gravitational waves in AMR

During inspiraling and merging of binary compact objects, gravitational wavelength gradually decreases (the frequency increases). Propagation of gravitational waves is accurately computed only in the case that the grid spacing is at least by 1 order of magnitude smaller than the wavelength. Thus, the required grid resolution changes during the evolution. In the late inspiral phase in which $m_0\Omega = 0.03$–0.1, the wavelength is

$$\lambda = \frac{\pi}{\Omega} \approx 105\left(\frac{m_0\Omega}{0.03}\right)^{-1} m_0. \tag{60}$$

This implies that the grid spacing should be smaller than $\sim 10m_0$ for $m_0\Omega = 0.03$ and $\sim 3m_0$ for $m_0\Omega = 0.1$. By contrast, in the merger phase in which $m_0\Omega$ can be as large as ~ 0.3, the grid spacing has to be smaller than $\approx m_0$.

Another requirement for accurate computation of gravitational waves is that wave extraction has to be done in a wave zone. Thus, inspiral gravitational waveforms should be extracted in a region far from the source. On the other hand, merger waveforms may be extracted at a distance of $\sim 20m_0$ because the gravitational wavelength at the merger phase is 10–$15m_0$ (see Sec. IV).

Taking into account these requirements, we extract gravitational waves in the following manner. For the inspiral gravitational waveforms, the radius of the extraction is chosen to be 50–$70m_0$ in the present paper. The grid spacing at such radius is ~ 2–$3m_0$ in the present grid setting. For the merger gravitational waveforms, the radius of the extraction is ~ 20–$30m_0$. More specifically, the inspiral waveforms are extracted for $t_{\rm ret} \le t_{\rm sep}$, whereas the merger ones are done for $t_{\rm ret} \ge t_{\rm sep}$. Here, $t_{\rm ret}$ denotes retarded time defined by

$$t_{\rm ret} \equiv t - r - 2m_0 \log(r/m_0), \tag{61}$$

where r is the coordinate radius of the extraction and we assume $r \gg m_0$ for defining this retarded time. $t_{\rm sep}$ denotes a retarded time at which the orbital angular velocity of the binary motion becomes $m_0\Omega \sim 0.1$. In Sec. IV, we will show that this strategy is acceptable.

IV. NUMERICAL RESULTS

In the following three Secs. IV A, IV B, and IV C, we separately report numerical results for BH-BH, NS-NS, and BH-NS binaries, respectively. All the numerical results obtained by SACRA were performed on personal computers with a 2.4 or 2.6 or 3.0 GHz Opteron processor and 4 or 8 GBytes of memory. Many of numerical simulations were performed both in the F_i-BSSN and $\tilde{\Gamma}^i$-BSSN formalisms. Although both formalisms give similar results, slight quantitative difference is also found. (The difference results primarily from the difference in the gauge conditions adopted in both formalisms.) In each following section, we basically present the results in the $\tilde{\Gamma}^i$-BSSN formalism. In the presence of remarkable quantitative difference between two results, we will notice the difference.

A. BH-BH binaries

The first step is to validate the Einstein equations solver of SACRA. For this purpose, we performed simulations of BH-BH binaries of equal mass. Because many simulations have been already performed for the equal-mass binary in the past three years (see Sec. I for review), it is possible to compare our numerical results with the previous ones and to check the validity of our code.

1. Initial condition

Following Ref. [23], as initial conditions, we adopt quasi-equilibrium states of BH-BH binaries in corotating circular orbits, which are computed by Cook and Pfeiffer [41] (see also [42,43]) in the conformal-thin sandwich framework. The data can be obtained from a website [44]. Cook, Pfeiffer, and their collaborators have computed a wide variety of quasi-equilibrium states by a spectral method with high accuracy. Among many quasi-equilibria they computed, we pick up the corotating models with labels $d = 13$, 16, and 19 (see Table I for key quantities of these initial conditions) following a previous work [23]. These initial conditions are computed in an excision method [41], and hence, no data is present inside apparent horizons. We simply adopt a third-order Lagrangian interpolation to provide a spurious data inside the apparent horizons. As shown in Refs. [45,46], this quite simple method is acceptable because the spurious information inside the apparent horizons does not propagate outward. Indeed, no trouble was found also in our simulations. As shown in Ref. [23], BH-BH binaries orbit for about 1.5, 2.5, and 4.5 times before formation of common apparent horizon for $d = 13$, 16, and 19, respectively.

TABLE I. Parameters for BH-BH binaries in quasicircular states. We list the ADM mass (M_0), angular velocity (Ω_0), angular momentum (J_0), and a spin parameter of binary (χ). All these quantities are scaled with respect to m_0, which is the sum of irreducible mass of two BHs at $t = 0$.

d	M_0/m_0	$m_0\Omega_0$	J_0/m_0^2	χ
13	0.9858	0.05617	0.875	0.054
16	0.9875	0.04164	0.911	0.040
19	0.9890	0.03245	0.951	0.032

2. Setting

The simulations were performed changing the grid resolution and grid structure for a wide range, to examine convergence of the numerical results as well as to check dependence of the results on locations of outer and refinement boundaries (see Table II for the key parameters of the grid structure). The numerical experiments were extensively performed, in particular, for $d = 19$. For all the cases, the grid spacing in the vicinity of BHs is between $\approx m_1/12$ and $\approx m_1/18$ (m_1 is the irreducible mass of each BH), and the outer boundaries along each axis are located at 2–4 times of gravitational wavelength at $t = 0$ (which is denoted by λ_0).

Instead of employing the solution of quasi-equilibrium states for α and β^k at $t = 0$, we initially give

$$\alpha = W \quad \text{and} \quad \beta^k = 0. \tag{62}$$

We also performed simulations with the quasi-equilibrium gauge as initial condition for a few models (see Appendix B). Switching the initial condition for α from Eq. (62) to the quasi-equilibrium one does not change the numerical results significantly. By contrast, using the quasi-equilibrium solution for β^k, the orbital trajectory of BHs (in coordinate description) are significantly modified for the case that the $\tilde{\Gamma}^i$-BSSN formalism is employed (see also Ref. [46]). Specifically, the orbit becomes elliptical in the coordinate description. By contrast, for the case that the F_i-BSSN formalism is employed, numerical results depend only weakly on the initial condition. In both cases, physical results (e.g., gravitational waveforms and state of the BH finally formed) depend very weakly on the initial condition. The results are briefly presented in Appendix B.

The elliptical orbit in the Γ-freezing gauge is likely to result simply from a gauge effect. However, the gauge could affect the physical results (see discussion below), and hence, it is better to fix the condition for studying convergence of the numerical results for different grid resolutions. In the present paper, we employ the gauge condition of Eq. (62) at $t = 0$ following Ref. [46], and discuss the convergence and dependence of numerical results on the grid structure fixing the initial condition for α and β^i.

Most of the simulations were performed with $N = 30$ or 24. Required memories for runs with $N = 30$ and 24 are at most about 2.8 and 1.6 GBytes, respectively, when the $\tilde{\Gamma}^i$-BSSN formalism is employed. When the F_i-BSSN formalism is employed, we do not have to introduce the auxiliary variable B^i, and hence, the memory is slightly saved. In both cases, the simulations are feasible on inexpensive personal computers with 4 GBytes of memory. A few simulations were performed for $N = 36$, but it is still feasible by personal computers with 8 GBytes of memory. The computation time required for run 19a, for which binary orbits for about 4.5 times before the onset of merger, is about two weeks on a 2.4 GHz Opteron machine, even with no parallelization. For $d \leq 16$, the required computational time is at most 10 days even for $N = 30$.

3. Evolution of BHs and final outcome

Figure 1(a) plots orbital trajectories of one of two BHs for runs 19a, 16a, and 13a. The trajectories from $t = 0$ to

TABLE II. Parameters of grid structure for simulations of BH-BH binaries. In the column named "Levels," the number of total refinement levels is written. (In the bracket, the numbers of coarser and finer levels are written.) Δx is minimum grid spacing, $\Delta x_{\rm QNM}$ the grid spacing at which the quasinormal mode of gravitational waves are extracted, $\Delta x_{\rm ins}$ the grid spacing at which inspiral gravitational waves are extracted, m_1 the irreducible mass of each BH, L the location of outer boundaries along each axis, and λ_0 the gravitational wavelength at $t = 0$. Run names with "F" denote that the simulations were performed with the F_i-BSSN formalism, and otherwise, the simulations were performed with the $\tilde{\Gamma}^i$-BSSN formalism.

Run	"d"	Levels	N	$\Delta x/m_1$	$L/m_0(L/\lambda_0)$	$\Delta x_{\rm QNM}/m_0$	$\Delta x_{\rm ins}/m_0$
13a, aF	13	9 (5 + 4)	24	0.0566	174 (3.1)	0.46, 0.91	1.82
13b	13	9 (5 + 4)	20	0.0680	174 (3.1)	0.55, 1.09	2.18
13c	13	9 (5 + 4)	16	0.0850	174 (3.1)	0.68, 1.36	2.72
13d	13	9 (5 + 4)	24	0.0708	217 (3.9)	0.57, 1.13	2.24
16a, aF	16	9 (5 + 4)	30	0.0578	222 (2.9)	0.46, 0.92	1.84
16b, bF	16	9 (5 + 4)	24	0.0578	178 (2.3)	0.46, 0.92	1.84
16c, cF	16	9 (5 + 4)	24	0.0723	222 (2.9)	0.58, 1.16	2.32
16d, dF	16	9 (5 + 4)	20	0.0868	222 (2.9)	0.70, 1.39	2.78
19a, aF	19	9 (5 + 4)	30	0.0587	225 (2.4)	0.47, 0.94	1.88
19b, bF	19	9 (5 + 4)	24	0.0587	180 (1.9)	0.47, 0.94	1.88
19c, cF	19	9 (5 + 4)	24	0.0733	225 (2.4)	0.59, 1.18	2.35
19d, dF	19	9 (5 + 4)	20	0.0880	225 (2.4)	0.71, 1.41	2.82
19e, eF	19	10(6 + 4)	24	0.0587	360 (3.8)	0.47, 0.94	1.88
19f	19	9 (5 + 4)	36	0.0587	270 (2.9)	0.47, 0.94	1.88
19g	19	9 (5 + 4)	24	0.0880	270 (2.9)	0.71, 1.41	2.82

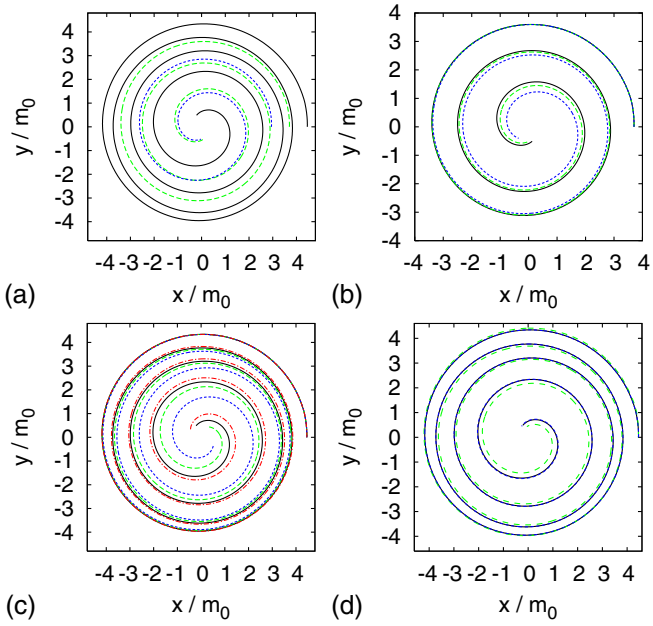

FIG. 1 (color online). (a) Coordinate trajectories of a BH from $t = 0$ to the time at which the common apparent horizon is first formed for runs 19a (solid curve), 16a (long-dashed curve), and 13a (dashed curve). (b) The same as (a) but for runs 16a (solid curve), 16c (long-dashed curve), and 16d (dashed curve). (c) The same as (a) but for runs 19a (solid curve), 19b (dotted-dashed curve), 19c (long-dashed curve), and 19d (dashed curve). (d) The same as (a) but for runs 19a (solid curve), 19aF (long-dashed curve), and 19f (dashed curve). The orbits for runs 19a and 19f overlap approximately.

the time at which common apparent horizon is first formed are drawn. This shows that for $d = 19$, 16, and 13, the BH-BH binaries orbit approximately for 4.3, 2.75, and 1.75 times, respectively. The result for $d = 19$ approximately agrees with that of Ref. [23], whereas for $d = 16$ and 13, our results are by about a quarter orbit longer (see discussion below). As pointed out in Ref. [23], the trajectory for $d = 19$ looks slightly eccentric, whereas for $d = 16$ and 13, the eccentricity is not very outstanding.

Figure 1(b) and 1(c) are the same as Fig. 1(a) but for runs 16a, 16c, 16d and for runs 19a, 19b, 19c, and 19d, respectively. These two figures compare the trajectories in different grid resolutions but with the same arrangement for locations of refinement boundaries. They show that for the finer grid resolutions, the number of orbits increases, i.e., the time at which common apparent horizon is first formed (hereafter referred to as the merger time $T_{\rm AH}$) is longer. The reason for this feature is that numerical dissipation is larger for the simulations with poorer grid resolutions, and as a result, the decrease rate of orbital separation is spuriously enhanced. However, Fig. 1(b) indicates that the difference in the merger time is not very large for $d = 16$, and suggests that the numerical results are close to convergence. For $d = 13$ and 16, we infer that in the best-resolved runs, the merger time is determined within an error of $\sim 2m_0$ and $10m_0$, respectively. By contrast, for $d = 19$, the merger time may be underestimated by $\sim 50m_0$ even for run 19a. This point will be revisited in Sec. IV A 4.

The trajectory of BHs for run 16b is very similar to that for 16a (we do not plot it because it approximately agrees with that for run 16a). By contrast, the trajectory for run 19b does not agree well with that for run 19a (see also Table III for the merger time which shows that the difference in the merger time is $\sim 20m_0$). This indicates that for the simulations started from small initial orbital separations ($d \leq 16$), our choice for the location of outer and refinement boundaries and for the grid structure is appropriate. On the other hand, for a simulation started from a large initial separation as $d = 19$, a careful choice of the grid structure is necessary. In addition, the trajectory and merger time depend on the gauge condition; see comparison between the results with F_i-BSSN and $\tilde{\Gamma}^i$-BSSN formalisms, for which the chosen spatial gauges are different (see Sec. IV A 4).

Figure 2 plots $M_{\rm irr}/m_0$, $C_e/4\pi m_0$, and C_p/C_e as functions of time for common apparent horizon for $d = 16$ and 19. The asymptotic values of these quantities characterize properties of the final state of the formed BHs, as described in Sec. II C. Figure 2 shows that all the quantities approach approximately to constants and the formed BHs relax to a stationary state irrespective of initial orbital separation. An oscillation associated with numerical error is seen, but the amplitude of such oscillation is within $\sim 0.1\%$. Thus, the final stationary state of the BHs is determined with a small error of $\lesssim 0.1\%$ (except for runs performed with a poor grid resolution such as runs 16dF, 19d, and 19dF, for which values for these quantities do not approach to constants).

In Table III, we summarize key numerical results about the formed BHs. We note that the last column of Table III denotes the refinement level for which the properties of the common apparent horizon are determined; "$L - 1$" and "$L - 2$ denote the finest and second-finest levels, respectively. For the case that volume of the finest refinement domain is so small that the radius of the common apparent horizon is larger than the domain size, we have to determine it in the second-finest one for analyzing the properties of the BH. Because its resolution is poorer than that of the finest one, we have to keep in mind that systematic error for the results marked with "$L - 2$" is larger than that with "$L - 1$." In particular, a substantial error appears to be always present for the estimated mass; by comparing the results determined in the finest and second-finest levels, we find that the mass is underestimated by $\sim 0.2\%$ when the results in the second-finest level is used.

Although such systematic error is present, Table III shows that the results for the properties of the BH finally formed depend only weakly on the grid resolution, grid structure, chosen formalism, and gauge condition: The final mass determined both from $M_{\rm irr}$ and C_e is

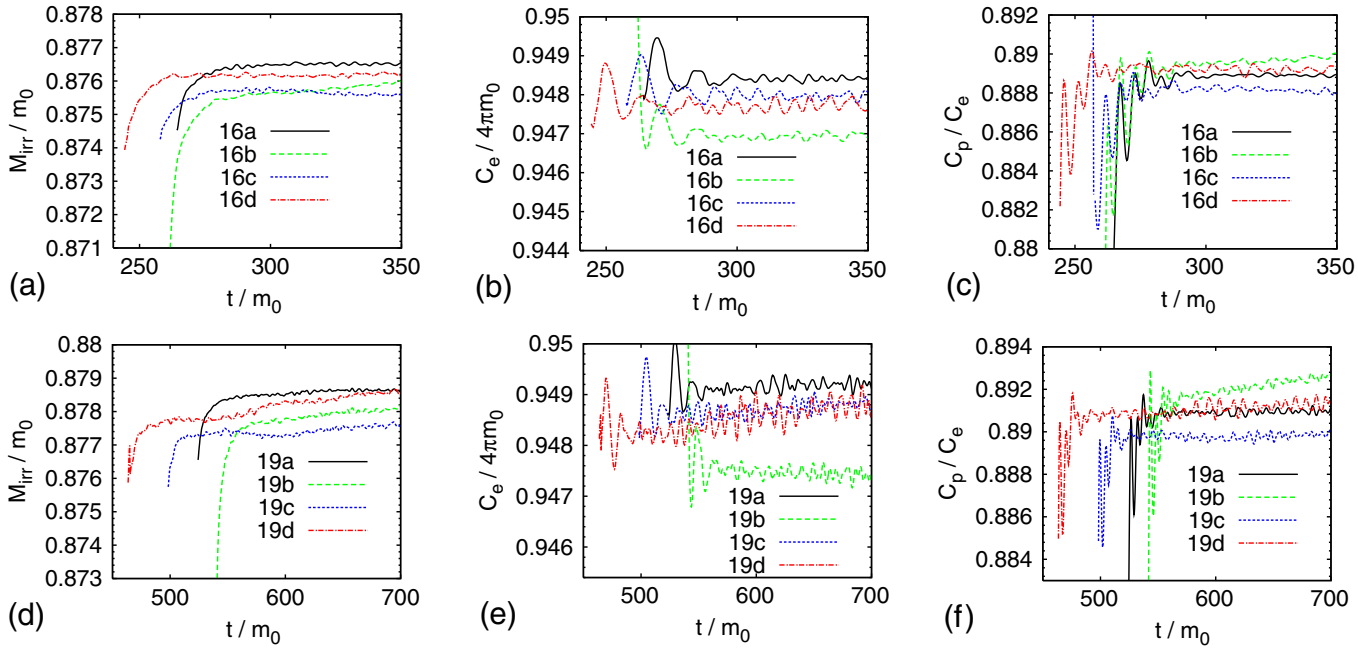

FIG. 2 (color online). (a) $M_{\rm irr}/m_0$ as a function of time for a BH formed after merger for run 16a–16d. (b) The same as (a) but for $C_e/4\pi m_0$. (c) The same as (a) but for C_p/C_e. (d) The same as (a) but for runs 19a–19d. (e) The same as (b) but for runs 19a–19d. (f) The same as (c) but for runs 19a–19d. We note that numerical error of the results for runs 16b and 19b is larger than those for runs 16a and 19a because the apparent horizon for these runs is determined from the data of the second-finest AMR level.

$(0.948 \pm 0.001)m_0$ for $d = 13$ and 16, and $(0.949 \pm 0.001)m_0$ for $d = 19$. The final spin determined from C_p/C_e is 0.71 ± 0.01 for $d = 13$ and 16 and 0.70 ± 0.01 for $d = 19$. These results agree with those of Ref. [23] within estimated numerical error.

In our results, the final masses of the BHs computed both from C_e and Eq. (47) agree within $\approx 0.1\%$ error. Because two values are determined by two independent methods, this agreement also indicates that the BH mass is determined within $\sim 0.1\%$ error.

Another point worth noting is that the final mass and spin depend very weakly on the initial orbital separation. This is natural because the merger should start at an approximately unique point in the vicinity of an innermost stable orbit at which the energy and angular momentum of the binary system is approximately identical independent of the initial orbital separation. Note that slight difference in spin of individual BHs could cause a slight difference of the location of the innermost stable orbit. However, the magnitude of the spin is small and the effect is minor. Hence, after the merger sets in, the evolution path toward the final state and the final outcome should depend only weakly on the initial separation.

4. Merger time

In contrast to the results for the mass and spin of the BHs finally formed, the merger time depends on the grid resolution for $d = 16$ and, in particular, for $d = 19$. Because it increases systematically with improving the grid resolution, the smaller merger time is a result due to the fact that numerical dissipation is larger for the poorer grid resolutions. To see the dependence of the merger time on the grid resolution, we plot $T_{\rm AH}$ as a function of h_{L-1}^2 in Fig. 3. It is found that for a given location of outer and refinement boundaries (compare the results for 16a, 16c, 16d and for 19a, 19c, 19d, respectively), $T_{\rm AH}$ systematically increases in a manner better than second-order convergence.

The merger time for runs 16a and 16b (and also for runs 13a and 13b), for which the finest grid resolution is the same whereas the locations of outer and refinement boundaries at each level are different, agrees approximately with each other. This implies that the grid structures for these runs are well suited for an accurate simulation; the outer boundaries are located far enough to exclude spurious effects associated with the finite size of computational domain, and also, the refinement boundaries and the domain size of each level are appropriately chosen. We can conclude that the results depend primarily on the finest grid resolution as long as $N \geq 24$ and $L \gtrsim 2\lambda_0$ for $d = 13$ and 16.

In contrast to the results for $d = 13$ and 16, the merger times for runs 19a and 19b does not agree well with each other. This implies that the orbital evolution of BHs depends either on the location of outer boundaries or on the location of refinement boundaries. For $d = 19$, the BHs orbit for ~ 4.5 times. For such a long run, a small error is likely to be accumulated, leading to a non-negligible error.

TABLE III. Numerical results for simulations of BH-BH binaries. We list the time at which a common apparent horizon is formed ($T_{\rm AH}$), final value of the irreducible mass for the common apparent horizon ($M_{\rm irr}$), final value of the ratio of the polar circumferential length to the equatorial one (C_p/C_e), final BH mass estimated from the equatorial circumferential length ($C_e/4\pi$), BH mass estimated from $M_{\rm irr}$ and C_p/C_e ($M_{\rm BHf}$), final spin parameter of the BH estimated from C_p/C_e, and energy and angular momentum carried away by gravitational waves (ΔE and ΔJ). "—" denotes that the values of the area and C_p/C_e do not relax to constants because of the poor grid resolution. The last column denotes the refinement level in which the common apparent horizon is determined. "1" and "2" are the finest and second-finest levels, respectively. For runs 16dF, 19cF, 19d, and 19dF, the area and the circumferential length of the apparent horizon vary with time and the values are not determined with a good accuracy.

Run	$T_{\rm AH}/m_0$	$M_{\rm irr}/m_0$	C_p/C_e	$C_e/(4\pi m_0)$	$M_{\rm BHf}/m_0$	a	$\Delta E/m_0$	$\Delta J/J_0$	Level
13a	125.3	0.873	0.887	0.946	0.946	0.712	0.034	0.24	$L-2$
13aF	125.7	0.873	0.884	0.948	0.948	0.720	0.034	0.24	$L-1$
13b	123.8	0.872	0.888	0.946	0.945	0.710	0.034	0.24	$L-2$
13c	122.3	$\sim$0.873	—	0.944	—	—	0.033	0.23	$L-2$
13d	123.8	0.871	0.884	0.947	0.946	0.720	0.033	0.23	$L-1$
16a	256.8	0.876	0.889	0.948	0.948	0.707	0.035	0.27	$L-1$
16aF	253.6	0.876	0.888	0.948	0.949	0.709	0.035	0.26	$L-1$
16b	257.1	0.876	0.889	0.947	0.948	0.707	0.035	0.27	$L-2$
16b'	255.4	0.876	0.889	0.948	0.949	0.707	0.035	0.27	$L-1$
16bF	268.6	0.876	0.888	0.948	0.948	0.709	0.035	0.26	$L-1$
16c	250.2	0.876	0.888	0.948	0.949	0.710	0.034	0.26	$L-1$
16cF	245.3	0.877	0.889	0.949	0.949	0.707	0.033	0.25	$L-1$
16d	237.0	0.876	0.889	0.948	0.948	0.707	0.035	0.27	$L-1$
16dF	220.7	$\approx$ 0.881	$\approx$ 0.895	$\approx$ 0.949	$\approx$ 0.949	$\approx$ 0.69	0.029	0.23	$L-1$
19a	516.7	0.879	0.891	0.949	0.950	0.702	0.036	0.29	$L-1$
19aF	499.3	0.878	0.891	0.949	0.950	0.703	0.035	0.28	$L-1$
19b	535.9	0.878	0.892	0.947	0.948	0.699	0.036	0.29	$L-2$
19bF	582.8	0.877	0.890	0.949	0.949	0.706	0.035	0.29	$L-1$
19c	491.6	0.878	0.890	0.949	0.949	0.705	0.036	0.28	$L-1$
19cF	488.9	$\approx$ 0.882	0.893	$\approx$ 0.950	0.951	0.696	0.034	0.27	$L-1$
19d	456.8	$\approx$ 0.878	0.891	$\approx$ 0.948	0.949	0.701	0.034	0.27	$L-1$
19dF	449.1	$\approx$ 0.884	$\approx$ 0.898	$\approx$ 0.950	$\approx$ 0.950	$\approx$ 0.68	0.030	0.24	$L-1$
19e	535.9	0.878	0.892	0.947	0.948	0.699	0.036	0.29	$L-2$
19eF	582.8	0.877	0.890	0.949	0.949	0.705	0.035	0.29	$L-1$
19f	517.8	0.879	0.891	0.949	0.950	0.703	0.036	0.29	$L-1$
19g	452.3	0.878	0.890	0.949	0.950	0.704	0.034	0.27	$L-1$

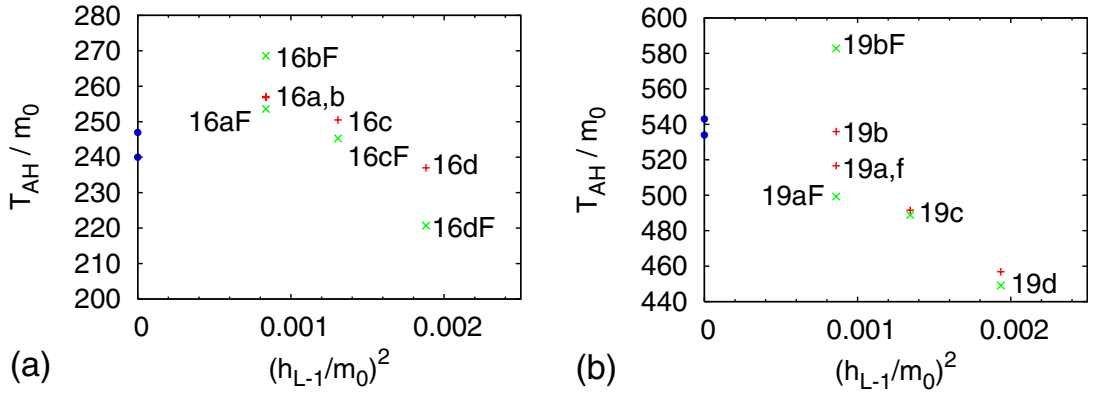

FIG. 3 (color online). Merger time $T_{\rm AH}/m_0$ as a function of the square of the finest grid resolution h_{L-1}^2 (a) for $d = 16$ and (b) for $d = 19$. The plus and cross denote the results in the $\tilde{\Gamma}^i$- and F_i-BSSN formalisms, respectively. Note that the plots for runs 16a and 16b and for runs 19a and 19f approximately overlap. The filled circles on the vertical axis denote a merger time predicted by the Taylor T4 formalism: The larger value denotes the value derived including the spin effect of BHs, whereas the smaller one is the value derived in the assumption of zero spin.

This disagreement gives us a caution that careful choice of the grid structure is necessary for the long-term evolution.

To clarify sources of the error in the merger time, we performed additional simulations for $d = 19$; runs 19e, 19f, and 19g (cf. Table II). For run 19e, the location of refinement boundaries is the same as that for run 19b, although outer boundaries are located twice far away from the center. We found that numerical results for run 19e agree very well with those for run 19b. This implies that the numerical results do not depend on the location of outer boundaries but on the location of refinement boundaries.

Additional runs 19f and 19g were performed to clarify the dependence of numerical results on the location of refinement boundaries, i.e., on the domain size of each refinement level. For these runs, the domain size of each refinement level is 1.2 times as large as that for runs 19a, 19c, and 19d, whereas the grid resolution for runs 19a and 19f and runs 19d and 19g are identical, respectively. We find that the results for runs 19f and 19g agree well with those for runs 19a and 19d, respectively, (see, e.g. Fig. 1(d) for the trajectories of runs 19a and 19f). By these results, we confirm that the location of refinement boundaries (and the size of domain) for run 19a is appropriately chosen: The error in the merger time comes primarily from the grid resolution. In any case, the present numerical results show that for simulations with a large initial orbital separation, a large domain size of the refinement levels is required.

The merger time for runs 19b and 19bF and for runs 16b and 16bF does not agree, although that for 19a and 19aF (see, e.g., Fig. 1(d)) and for 16a and 16aF, respectively, agrees in a much better manner. Note that the domain size of each refinement level for runs 16b and 16bF (19b and 19bF) is smaller than that for run 16a and 16aF (19a and 19aF); see Table II. This indicates that if the outer boundaries are too close or the domain size of each refinement level is too small, numerical results depend on the spatial gauge condition and/or the formulation. To check the dependence on the spatial gauge, we also performed a simulation in the $\tilde{\Gamma}^i$-BSSN formalism with $\eta_s \approx 0.5/m_1$ for $d = 16$ (run 16b'). With this change, the merger time changes by $\sim 2m_0$ (see Table III), which is a fairly large difference. This indicates that the difference in the spatial gauge seems to be the primary reason for discrepancy in the merger time.

Because the spatial gauge condition does not affect the slicing, one may think that the merger time should not depend on it. However, this is not correct in numerical computation because the spatial gauge condition determines physical grid spacing between two grid points even if the coordinate separation is the same. Namely, it affects the grid resolution physically, and hence, determines magnitude of numerical dissipation. Therefore, the merger time should depend on the chosen spatial gauge condition in general.

Because of the same reason, the physical location (not coordinate location) of outer and refinement boundaries depends on the spatial gauge condition. In particular, the physical size of the finest refinement level is likely to be sensitive to it. Thus, the magnitude of numerical error (and resulting merger time), in particular, around BHs where the curvature is large, depends on the spatial gauge condition.

Another characteristic feature in the simulation with the F_i-BSSN formalism is that the merger time depends more strongly on the grid resolution than the simulation in the $\tilde{\Gamma}^i$-BSSN formalism. For the poor-resolution simulations such as runs 16dF and 19dF, the merger time is much shorter than that for the corresponding finer-resolution simulations, and the quantities for the formed BHs after the merger are not determined accurately. Probably, this is also due to the fact that in the chosen spatial gauge condition, the BHs are not resolved well.

All these results suggest that with the F_i-BSSN formalism, systematic errors associated with a finite location of outer boundaries and/or finite grid resolutions are larger. However, in the case that the appropriate location of the outer boundaries and the appropriate grid resolution are chosen, both the F_i-BSSN and $\tilde{\Gamma}^i$-BSSN formalisms provide approximately the same result.

Extrapolating the value of $T_{\rm AH}$ to the limit $h_{L-1} \to 0$ for runs 16a and 16c and for runs 16aF and 16cF assuming that the error in $T_{\rm AH}$ is proportional to h_{L-1}^2, the true value of $T_{\rm AH}/m_0$ is estimated to be ≈ 260. Thus, for the best-resolved runs 16a and 16aF, the merger time is computed with $\approx 2\%$ error. Extrapolating to $h_{L-1} \to 0$ for runs 19a and 19c, the true value of $T_{\rm AH}/m_0$ is estimated to be ≈ 560. Thus, even for the best-resolved runs 19a and 19f, the merger time is underestimated by $\approx 40m_0$. For such a long-term simulation, a better resolution is obviously required.

On the vertical axis of Fig. 3, we plot time at the onset of merger that is predicted by the Taylor T4 formalism. Here, we assume that the merger sets in when $m_0\Omega$ reaches 0.2. (The initial condition is chosen to be the orbit with $\Omega = \Omega_0$ for each model.) Thus, this value may be slightly smaller than $T_{\rm AH}$ because it takes time from the onset of merger to formation of common apparent horizon. We also note that the Taylor T4 formalism is not a good approximation for the orbital evolution near the innermost stable circular orbit [28].

For $d = 16$ and $d = 19$, the predicted merger time by the Taylor T4 formalism is $247m_0$ and $544m_0$, respectively. Therefore, the merger time determined by the extrapolation of the numerical results for $h_{L-1} \to 0$ agrees with the predicted value within error of $20m_0$. The predicted merger time is smaller than the numerical results. This seems to be reasonable because the definition of the merger time for the numerical results and for the Taylor T4 formalism is different, as mentioned above. Nevertheless, the error is not so large that we conclude that the Taylor T4 formalism pro-

vides a good approximate value for the merger time,which can be a guideline for analyzing the numerical results.

The derived merger time ($\sim 125m_0$ for $d = 13$, $\sim 260m_0$ for $d = 16$, and $\sim 560m_0$ for $d = 19$) is slightly longer than the results reported in Ref. [23] in which $T_{\rm AH}/m_0 = 109 \pm 4$ for $d = 13$, 228 ± 16 for $d = 16$, and 529 ± 22 for $d = 19$. Part of the reason is that the slicing is different between two groups. The possible other reasons may be that (i) our code is fully fourth-order-accurate whereas the code of Ref. [23] is not, and (ii) our code does not include Kreiss-Oliger-type dissipation term whereas in the simulation of Ref. [23], it is included and the dissipative effect may spuriously enhance the decrease rate of the orbital separation.

5. Gravitational waves

Figures 4(a) and 4(b) plot plus and cross modes of gravitational waves for runs 16a and 19a. As described in Sec. III C, the waveforms in the early inspiral phase are extracted at large radii $\approx 70m_0$, and those in the late inspiral and merger phases are at small radii ($\approx 30m_0$) of a small grid spacing. Then, we match two waveforms at a retarded time $t_{\rm ret} = t_{\rm sep}$. Specifically, we match the waveforms at $t_{\rm sep} \approx 225m_0$ for run 19a and $\approx 103m_0$ for run 16a. The phase of gravitational waves depends slightly on the extracted radii, and a small phase difference between two waveforms extracted at different radii is present for both runs; for runs 19a and 16a, the phase difference is $\approx 2.5m_0$ and $2.9m_0$, respectively. We correct these phase differences to constitute smooth waveforms shown in Fig. 4. This figure shows that our strategy can produce waveforms of a good quality.

As we noted in Sec. IV A 4, the merger time for runs 16a and 19a would be shorter than the true values, determined by extrapolation, by $\sim 5m_0$ and $\sim 40m_0$, respectively. Thus, in the waveforms shown in Fig. 4, such phase error is included. As mentioned above, to derive a waveform with sufficiently small phase error for run 19a, a simulation with a finer resolution is necessary.

To clarify the properties of the error associated with finite grid resolution, we generate Figs. 4(c) and 4(d). In these figures, we compare the plus mode of gravitational waves for runs 19a and 19c. To match the wave phases of two numerical results, we plot

$$h_+ \cos(0.3\pi) + h_\times \sin(0.3\pi) \tag{63}$$

as a function of $t_{\rm ret} + 14m_0$ for the result of run 19c in Fig. 4(c). It is found that the waveforms in the inspiral orbit for two runs agree well except for those in the last inspiral orbit. This indicates that for accurately computing gravitational waveforms in the early inspiral phase (in this case, from about 0.5th orbit to about 3rd orbit), the present choice of the grid resolution is acceptable.

Figure 4(d) compares the waveforms in the final inspiral and merger phases. In this figure, the waveform defined by

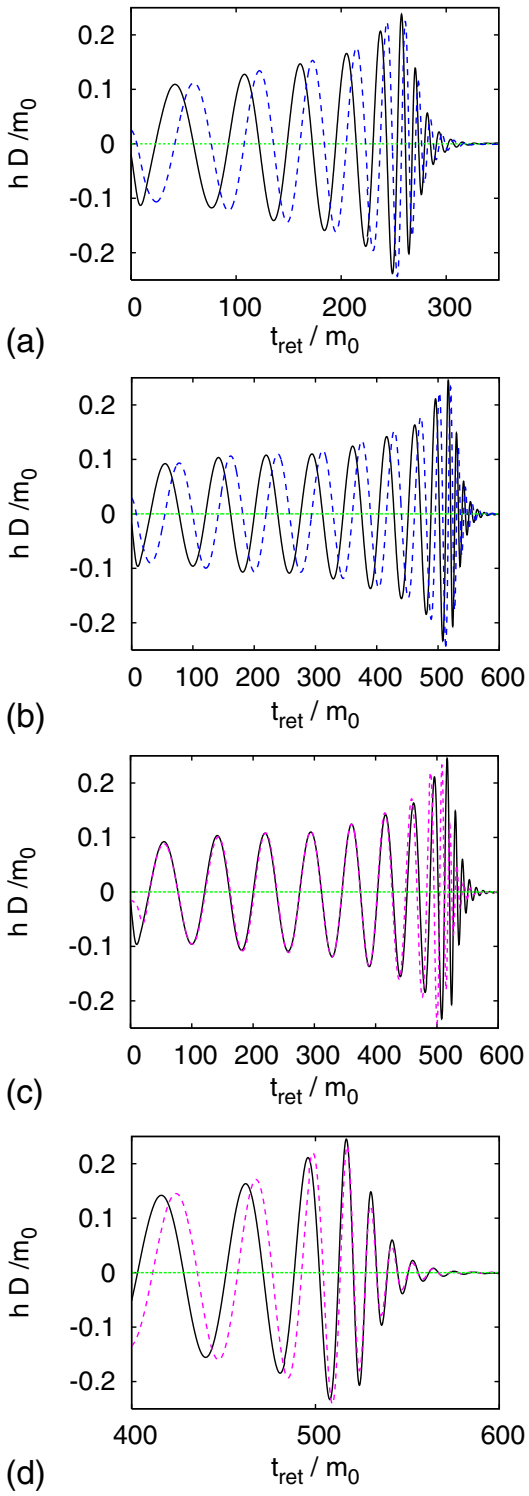

FIG. 4 (color online). Gravitational waveforms (a) for run 16a and (b) for run 19a. The solid and dashed curves are plus and cross modes, respectively. D denotes the distance from the source to an observer. (c) Plus mode of gravitational waves for runs 19a (solid curve) and 19c (dashed curve). For run 19c, the results are appropriately shifted to match the inspiral waveform (see text). (d) The same as (c) but here we compare ringdown waveforms.

Eq. (63) as a function of $t_{\rm ret} + 23m_0$ is plotted for run 19c to match the ringdown waveforms. The figure shows that the phase error is rapidly accumulated near the last inspiral phase. Also, we can see that the amplitude of the ringdown phase is underestimated for run 19c (by contrast, Fig. 4(c) shows that the amplitude in the inspiral phase depends weakly on the grid resolution). Thus, we conclude that in a run with a poor grid resolution, (i) the time duration for the inspiral phase near the last inspiral orbit is underestimated and (ii) the amplitude of the ringdown waveform is underestimated.

Figure 5(a) plots angular velocity computed from gravitational waveforms for runs 16a and 19a. Here, the angular velocity is derived from Ψ_4 by

$$\Omega(t) = \frac{1}{2}\frac{|\Psi_4(l=m=2)|}{|\int dt \Psi_4(l=m=2)|}, \tag{64}$$

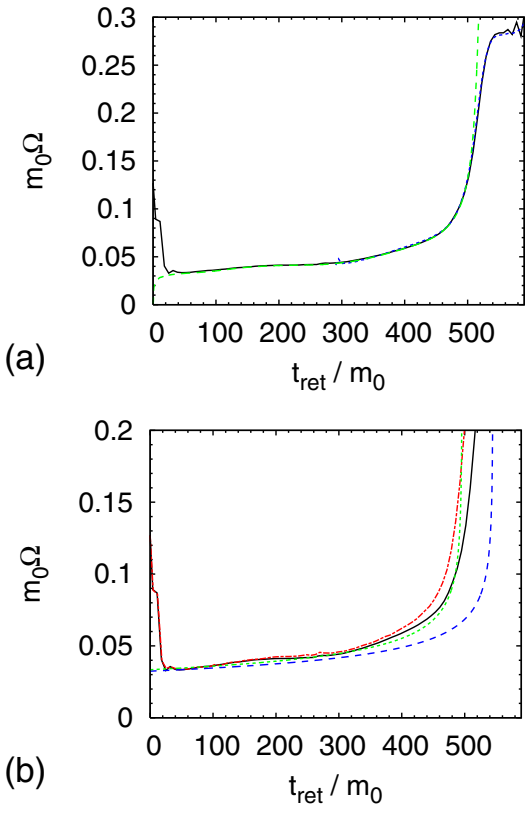

FIG. 5 (color online). (a) $m_0\Omega$ computed from gravitational waveforms for runs 19a (solid curve) and 16a (dashed curve). For run 16a, we plot $m_0\Omega$ as a function of $t_{\rm ret} + 258m_0$. The long-dashed curve denotes the results derived from the orbital motion of one of BHs. (b) Comparison of $m_0\Omega$ computed from gravitational waveforms with those derived from the Taylor T4 formalism for runs 19a (solid curve) and 19aF (dotted-dashed curve). The long- and short-dashed curves are results derived by the Taylor T4 formalism, drawn for the nonspinning equal-mass binary with $m_0\Omega(t=0) \approx 0.03245$ and 0.03345 at $t_{\rm ret} = 0$, respectively.

where $\Psi_4(l=m=2)$ is the $l=m=2$ mode of Ψ_4. We also derive it from the orbital motion of BHs for run 19a (the short-dashed curve of Fig. 5), and this result agrees well with that derived from Eq. (64). Thus, in this case, the coordinate trajectory approximately represents the physical trajectory (but this is not always the case; see Appendix B).

The curves for runs 16a and 19a agree approximately with each other, indicating that gravitational waveforms in the late inspiral phase depend very weakly on the initial condition as far as the initial value of $m_0\Omega_0 \lesssim 0.041$. Figure 5(a) also shows that the angular velocity does not increase monotonically in the early stage for run 19a. This implies that an eccentricity is present in the early stage. This is also pointed out in Ref. [23] in which the estimated eccentricity is $\sim$0.02. The curve of Fig. 5 is similar to that reported in Ref. [23]: Initially, $m_0\Omega \approx 0.033$, and then, it reaches a local maximum of $m_0\Omega \approx 0.040$. These results reconfirm that the eccentricity of the initial condition would be $\sim$0.02.

We compare the numerical results for $m_0\Omega(t)$ for runs 19a and 19aF with those derived from the Taylor T4 formalism in Fig. 5(b). Because we adopt corotating binary BHs as the initial conditions, the spin of each BH is not zero [43] and, thus, we take into account the spin effects in this analysis. In Fig. 5(b), the results by the Taylor T4 formalism are plotted for the case $m_0\Omega(t=0) = 0.03\,245 (= m_0\Omega_0)$ and 0.03 345. The figure shows that the numerical results agree approximately with the Taylor T4 curve of $m_0\Omega(t=0) = 0.03\,345$ besides a modulation associated with an elliptical orbital motion, but not very well with the curve of $m_0\Omega(t=0) = 0.03\,245$, which is approximately equal to the initial angular velocity for $d = 19$. There are at least two reasons for this discrepancy. The primary reason is that numerical dissipation associated with finite-differencing spuriously enhances the decrease rate of the orbital separation. Indeed, the merger time derived from the Taylor T4 formalism with $m_0\Omega(t=0) = 0.03\,245$ is by $\approx 50m_0$ longer than that with $m_0\Omega(t=0) = 0.03\,345$. The error of $50m_0$ agrees approximately with the possible error size for run 19a (cf. Sec. IV A 4). The other is that the initial condition is not exactly in a circular orbit but in an elliptical orbit for which the initial averaged angular velocity is not equal to $m_0\Omega_0 \approx 0.03\,245$ but slightly larger than it.

In the final phase of merger, ringdown gravitational waves associated with quasinormal modes are emitted. Perturbation studies predict their angular velocity and damping time scale for the nonaxisymmetric fundamental mode with $l = m = 2$ as [47]

$$M_{\rm BHf}\Omega_{\rm QNM} \approx 1.0[1 - 0.63(1-a)^{0.3}], \tag{65}$$

$$t_d \approx \frac{4(1-a)^{-0.45}}{\Omega_{\rm QNM}}. \tag{66}$$

For $a = 0.70$, $M_{\rm BHf}\Omega_{\rm QNM} \approx 0.56$. Because $M_{\rm BHf} \approx 0.95m_0$, the predicted value is $m_0\Omega_{\rm QNM} \approx 0.59$. Figure 5 shows that the numerical result of this value is ≈ 0.57 (note that the angular velocity of gravitational waves is 2Ω). Thus, the frequency of the quasinormal mode is computed with $\sim 3\%$ error.

Figure 6 plots the time evolution of gravitational wave amplitude defined by $(h_+^2 + h_\times^2)^{1/2}$ as a function of the retarded time for run 19a. For comparison, the amplitude for run 16a and those derived by the Taylor T4 formalism are shown together (see the figure caption for details). This figure shows that the amplitude for run 19a agrees with that in the Taylor T4 formalism with $\approx$ 10–20% error for $t_{\rm ret} \lesssim 300m_0$. The amplitude modulates with time in the early phase because of the presence of the orbital eccentricity. In the late phase, the amplitude of the numerical results is much larger than that in the Taylor T4 formalism. This is also seen in other numerical results (e.g., [23,28]), and our results are consistent with the previous results. The possible reason for this large amplitude is that the tidal deformation of BHs, which is not taken into account the Taylor T4 formalism, increases the attraction force between two BHs. This leads to the acceleration of inward motion and consequently to the speed-up of the orbital motion, resulting in the amplification of the gravitational wave amplitude.

6. Radiated energy and angular momentum, and their conservation

Total energy and angular momentum radiated by gravitational waves are listed in Table III (see ΔE and ΔJ). It is found that the radiated energy depends very weakly on the initial condition. This implies that most of the energy is radiated in the final merger phase; during inspiral from $m_0\Omega \approx 0.032$ (initial condition for model d19) to ≈ 0.056 (that for model d13), the energy is radiated only by ~ 0.002–$0.003m_0$. This fact is easily inferred from small difference in the ADM mass among three models of $d =$ 13, 16, and 19 (see Table I). Indeed, Table I shows that the difference in the ADM mass is $\sim 0.003m_0$ between the results for $d = 13$ and $d = 19$, which agrees approximately with the estimated radiated energy during the inspiral phase. The angular momentum is also radiated most efficiently in the final merger phase. However, it is also radiated by several percents in the late inspiral orbits in contrast to the energy. This is simply because the angular momentum of the binary system depends on the orbital separation more strongly than the energy.

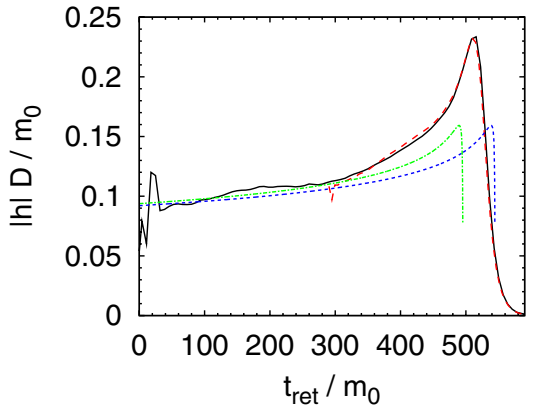

FIG. 6 (color online). Evolution of gravitational wave amplitude defined by $(h_+^2 + h_\times^2)^{1/2}$ as a function of retarded time for run 19a (solid curve). For comparison, amplitude for run 16a (dashed curve) is plotted as a function of $t_{\rm ret} + 258m_0$. The long-dashed and dotted-dashed curves denote wave amplitudes derived from the Taylor T4 formalism. These are drawn for the nonspinning equal-mass binary with $m_0\Omega(t = 0) \approx 0.03\,245$ and $0.03\,345$ at $t_{\rm ret} = 0$, respectively.

The total radiated energy derived here is significantly different from the results of Ref. [23] in particular for $d =$ 16 and 19. In their results, it depends strongly on the initial condition. However, we believe that our results are more reliable because of the following reasons: (i) As mentioned above, the total radiated energy should not depend strongly on the initial condition. Our results are consistent with this expectation; (ii) The sum of the BH mass finally formed and the total radiated energy should be equal to the initial ADM mass. Namely, the following relation should hold:

$$M_{\rm BHf} + \Delta E = M_0. \tag{67}$$

In our results, the left-hand side is $\approx 0.983m_0$ for $d = 16$ and $\approx 0.985m_0$ for $d = 19$, whereas the right-hand side is 0.9875 and 0.9890, respectively. Thus, the magnitude of the error is $\approx 0.5\%$. The left-hand side of Eq. (67) is systematically smaller than M_0, and hence, ΔE is likely to be underestimated due to numerical dissipation by $\sim 0.004m_0$. On the other hand, in the results of Ref. [23], the left-hand side of Eq. (67) is $(0.997 \pm 0.009)m_0$ for $d = 16$ and $(1.004 \pm 0.009)m_0$ for $d = 19$. Thus, these are larger than the left-hand side ($M_0 = 0.9875$ and 0.9890 for $d =$ 16 and 19) by 1–1.5%, and magnitude of the error increases with the increase of d. The reason seems to be that the total radiated energy is systematically overestimated for larger values of d. (As pointed out above, ΔE should not depend strongly on the initial condition, but in their results, ΔE steeply increases with increasing the value of d.)

The conservation relation for angular momentum is written by

$$M_{\rm BHf}^2 a + \Delta J = J_0. \tag{68}$$

For $d = 13$, 16, and 19, the error in the conservation relation defined by $1 - (M_{\rm BHf}^2 a + \Delta J)/J_0$ is $\sim 2\%$, 3%, and 4%, respectively, for the best-resolved runs. Thus, magnitude of the error is larger than that for the energy conservation. The left-hand side of Eq. (68) is always smaller than the initial value J_0. This implies that either a or ΔJ is underestimated. As mentioned above, ΔE is

TABLE IV. List of several quantities for irrotational binary NSs in quasi-equilibrium circular orbits. We show the compactness of each NS in isolation ($M_{\rm NS}/R_{\rm NS}$), gravitational mass of each NS in isolation ($M_{\rm NS}$), maximum density for each star ($\rho_{\rm max}$), total baryon rest mass (M_*), ADM mass at $t = 0$ (M_0), nondimensional angular momentum parameter (J_0/M_0^2), and angular velocity in units of M_0^{-1} ($M_0\Omega_0$). All these quantities are shown in units of $c = G = \kappa = 1$; in other words, they are normalized by κ appropriately to be dimensionless. We note that the mass, the radius, and the density can be rescaled to desirable values by appropriately choosing κ.

Model	$M_{\rm NS}/R_{\rm NS}$	$M_{\rm NS}$	$\rho_{\rm max}$	M_*	M_0	J_0/M_0^2	$M_0\Omega_0$
NS1616	0.160, 0.160	0.1478, 0.1478	0.152, 0.152	0.3200	0.2924	0.9584	0.0305
NS1416	0.140, 0.160	0.1363, 0.1478	0.118 0.152	0.3061	0.2810	0.9685	0.0289

underestimated. Thus, the error in ΔJ is likely to be the primary source of the underestimation.

B. NS-NS Binaries

For validating our new hydrodynamic code with the AMR algorithm, we first performed simulations for NS-NS binaries.

1. Initial condition

Following our previous works [3,4], we adopt NS-NS binaries of the irrotational velocity field in quasi-equilibrium circular orbits as initial conditions. The quasi-equilibrium state is computed in the so-called conformally flat formalism for the Einstein equations [48]. The irrotational velocity field is assumed because it is considered to be a good approximation of the velocity field for coalescing binary NSs in nature [49]. We employ the numerical solutions computed by Taniguchi and Gourgoulhon, which are involved in the LORENE library [50–52]. Specifically, we pick up two models computed in the polytropic EOS with $\Gamma = 2$ [51]; one is an equal-mass binary for which compactness of each NS is 0.16 and coordinate separation between two centers of mass is 45 km in the LORENE unit. The other is an unequal-mass binary for which compactness are 0.14 and 0.16, and coordinate separation between two centers of mass is 45 km in the LORENE unit. We simulate this to demonstrate that our code can follow unequal-mass binaries as well as equal-mass ones. We list several key parameters for these models in units of $c = G = \kappa = 1$ in Table IV.

2. Setting

Simulations were performed for a variety of grid structures and grid resolutions (see Table V). For model NS1616, we also performed a simulation using Shibata's code in which a nonuniform unigrid is adopted. This code is the same as that presented in Ref. [29,30]; the Einstein evolution equations are solved in the F_i-BSSN formalism with a fourth-order finite differencing in space, and the hydrodynamic equations are solved in the same scheme as SACRA. The third-order Runge-Kutta scheme is employed for evolution forward in time.

Grid resolutions and grid sizes in the simulations with SACRA are listed in Table V. For all the cases, the NSs are covered by the finest and second-finest levels (central region of each NS is covered by the finest level and the region near the surface is covered by the second-finest level). For models NS1616a–NS1616c, the simulations were performed both in the F_i-BSSN and $\tilde{\Gamma}^i$-BSSN formalisms, whereas the simulations for models NS1616s, NS1616d, NS1616e, and NS1416a–c were done in the $\tilde{\Gamma}^i$-BSSN formalism. The best-resolved runs for models NS1616 and NS1416 are NS1616s and NS1416a, respectively.

TABLE V. The same as Table II but for simulations of models NS1616 and NS1416. Δx is the minimum grid spacing, $R_{\rm diam}$ the coordinate length of the semi-major diameter of NSs, L the location of outer boundaries along each axis, λ_0 the gravitational wavelength at $t = 0$, and $\Delta x_{\rm gw}$ the grid spacing at which gravitational waves are extracted. $M_{\rm NS}$ is the ADM mass of larger NS in isolation, which is 0.1478 in the present units. For models NS1616a–NS1616c, simulations are performed both in the F_i-BSSN and $\tilde{\Gamma}^i$-BSSN formalisms.

Run	Levels	N	$\Delta x/M_{\rm NS}$	$R_{\rm diam}/\Delta x$	$L/M_0(L/\lambda_0)$	$\Delta x_{\rm gw}/M_0$
NS1616s	8 (3 + 5)	36	0.068	130	158 (1.53)	1.09
NS1616a, aF	8 (3 + 5)	30	0.081	108	158 (1.53)	1.31
NS1616b, bF	8 (3 + 5)	24	0.101	87	158 (1.53)	1.64
NS1616c, cF	8 (3 + 5)	20	0.122	67	158 (1.53)	1.97
NS1616d	7 (3 + 4)	30	0.135	65	131 (1.27)	1.09
NS1616e	7 (3 + 4)	24	0.169	52	131 (1.27)	1.37
Shibata	—	—	0.147	60	106 (1.03)	1.09
NS1416a	8 (3 + 5)	30	0.081	100	164 (1.51)	1.37
NS1416b	8 (3 + 5)	24	0.101	87	164 (1.51)	1.71
NS1416c	8 (3 + 5)	20	0.122	67	164 (1.51)	2.05

For the initial values of α and β^i, we employ those of the quasi-equilibrium solutions. Even when such initial condition is adopted in the Γ-freezing gauge condition, the orbital eccentricity appears to be not as large as that in the BH-BH-binary case. The value of η_s in the Γ-freezing gauge is set to be $\approx 1.7/M_0$ irrespective models. ($\eta_s = 0.5$ in units of $c = G = \kappa = 1$.)

3. Evolution of NSs and the final outcome

Figure 7(a) plots orbital trajectories for one of two NSs for runs NS1616s, a, b, and c. Here, the trajectories of the NSs are determined by tracking location of the maximum value of ρ_*. Note that for these runs, the locations of outer and refinement boundaries are the same, although the grid resolution is different. This figure shows that the binary experiences $\approx 9/4$, $10/4$, $11/4$, and $\lesssim 3$ orbits before the onset of merger for runs NS1616c, b, a, and s, respectively. For finer grid resolutions, the number of orbits is systematically larger, because numerical dissipation of angular momentum and energy is smaller. Figure 7(a) indicates that convergence of numerical results for $h_{L-1} \to 0$ appears to be not very fast, and for $h_{L-1} \to 0$, the number of orbits would be larger than 3 (see Fig. 11 and related discussion below).

Figure 7(b) compares orbital trajectories for runs NS1616b–d, and run by Shibata's code. For these runs, the finest grid spacing is $\Delta x/M_{\rm NS} = 0.101$, 0.122, 0.135, and 0.147, respectively. Although the grid resolution of the finest level for NS1616c is better than that for NS1616d (and also for run by Shibata's code), the merger time for NS1616c is shortest among four runs, and hence, the numerical dissipation is most serious in this run. (The merger time $T_{\rm AH}$ is defined in the same manner as that in the BH-BH binary case.) The reason for this is that for NS1616d, most of the NS is covered by the finest level (for run by Shibata's code, the entire region of the NS is covered by the finest grid), whereas for NS1616c, a relatively wide region of the NS is covered by the second-finest level: Dissipative effects of the second-finest level is much larger than that of the finest one, and hence, they spuriously enhance the decrease rate of orbital separation. This suggests that it is desirable to cover the entire region of the NSs by the finest level. However, to do this with a sufficient grid resolution, it is necessary to take a large number of grid points in the finest level. This is not desirable from the viewpoint of computational cost. We tried to perform simulation using several grid structures and found that an optimistic choice is that the finest level approximately covers about two-thirds of the NSs, from the viewpoints of grid resolution and computational cost. The grid structure for runs NS1616a–c and NS1416a–c is selected due to this reason.

Figure 7(c) plots orbital trajectories for more massive NS for runs NS1416a–c. This figure is similar to Fig. 7(a), and indicates that slight mass difference does not change

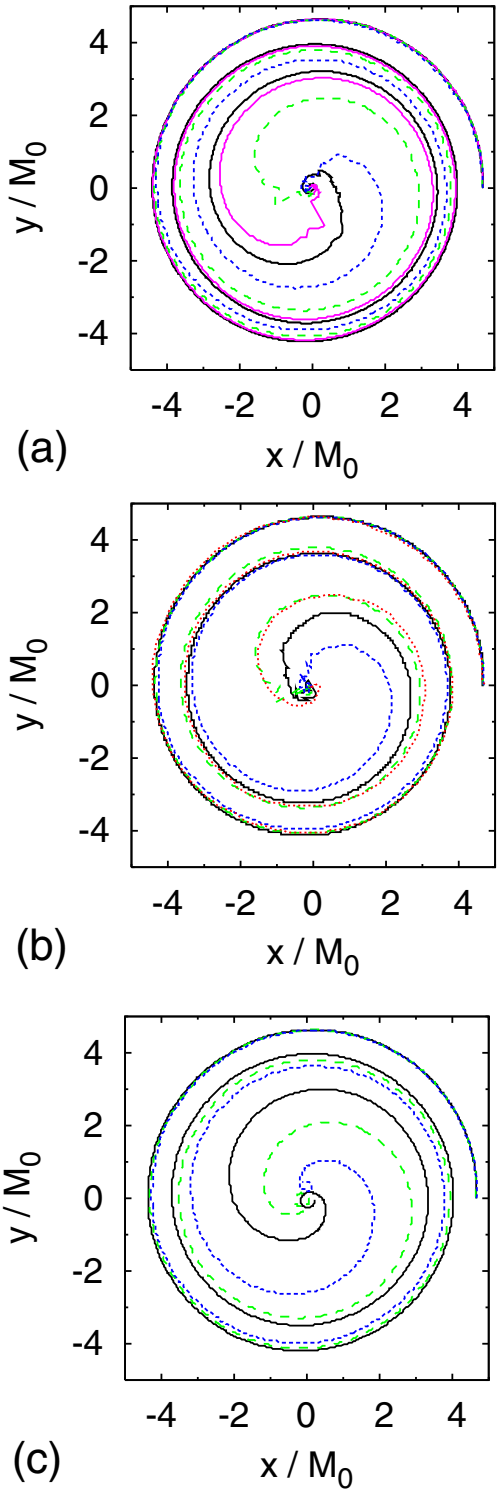

FIG. 7 (color online). (a) Orbital trajectories of an NS to formation of apparent horizon for runs NS1616s (thick solid curve), NS1616a (solid curve), NS1616b (long-dashed curve), and NS1616c (dashed curve). (b) The same as (a) but for runs NS1616d (solid curve), NS1616b (long-dashed curve), NS1616c (dashed curve), and for run by Shibata's code (dotted curve). (c) The same as (a) but for runs NS1416a (solid curve), NS1416b (long-dashed curve), and NS1416c (dashed curve). In this case, the trajectories for more massive NS are plotted.

qualitative properties for the orbital trajectories and convergence. As in the case of model NS1616, the merger time depends strongly on the grid resolution and convergence is not achieved even with the best-resolved run.

For models NS1616 and NS1416, a BH is soon formed after the onset of merger. This is reasonable because the total rest mass of these systems is more than 1.6 times as large as the maximum rest mass of nonrotating NSs (≈ 0.180) for the given EOS. We note that this result agrees well with our previous result obtained in the simulation with the Γ-law EOS and $\Gamma = 2$ [4] (see also a recent work by the Illinois group which confirms our result [7]).

The present code can follow the evolution of the formed BH for a long time stably. We find that $\approx 99.99\%$ of the total rest mass is swallowed by the BH for model NS1616 (cf. Figure 9). This is due to the facts that (i) specific angular momentum for most of the material at the onset of merger is not large enough to escape from capturing by the BH and (ii) there is no mechanism for transporting angular momentum outward in the merger of equal-mass binaries. This result agrees again with our previous result [4], and also, with a recent result by the Illinois group [7].

By contrast, a disk is formed for model NS1416. The rest mass for run NS1416a is $\sim 2\%$ of the total rest mass when we stopped the simulation (see Figs. 8 and 9 and Table VI). The disk formation results primarily from the mass difference of two NSs: Just before the merger, the smaller-mass NS is tidally disrupted by the larger-mass companion (see Fig. 8). Because of asymmetry in the mass distribution, angular momentum is subsequently transported, and the tidally disrupted material can spread outward. Because the specific angular momentum of such material is $\approx 2.5J_0/M_0$ and larger than that at the innermost stable circular orbit around the formed rotating BH, a compact disk is formed (see the last panel of Fig. 8). The maximum density of the disk is $\approx 10^{-4}$ in the present units, which is $\sim 1/1000$ of the maximum density of the NSs before merger (i.e., $\sim 10^{12}$ g/cm^3 in the cgs units if we assume that the maximum density of the NS is 10^{15} g/cm^3). Figure 8 shows that the material of the disk is located in a small region whose coordinate radius is ~ 3–$6M_0$. This is a result of small averaged specific angular momentum of the disk, $2.5J_0/M_0 \approx 2.4M_{\rm BHf}$ where $M_{\rm BHf}$ is the mass of the BH finally formed, which is $\approx 0.97M_0$ (see below and Table VI). Such compact disk can be formed due to the fact that the formed BH is rapidly rotating with the spin parameter $a \gtrsim 0.8$; the specific angular momentum for the innermost stable circular orbit around a Kerr BH is $j_{\rm ISCO} \approx 2.38M_{\rm BHf}$ for $a = 0.8$. (Note that $j_{\rm ISCO}/M_{\rm BHf} \approx 3.46$, 2.59, and 2.10 for $a = 0$, 0.7, and 0.9, respectively.)

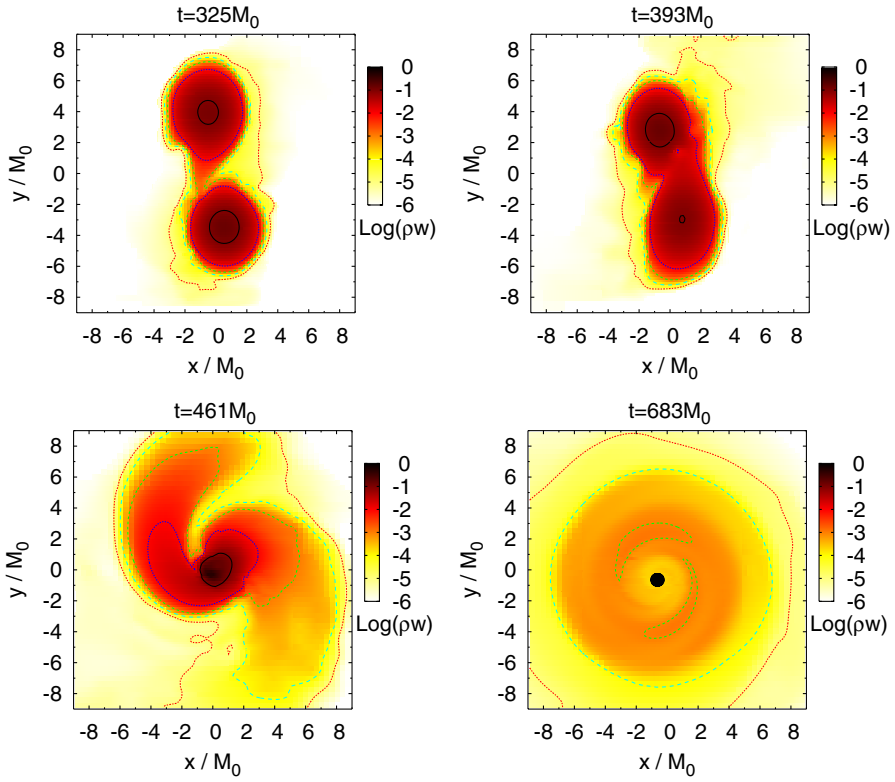

FIG. 8 (color online). Snapshots of density contour curves and density contrasts from merger phase to formation of a BH for run NS1416a. The contour curves are plotted for $\rho w = 10^{-i}$, where $i = 2, 3, \cdots, 6$ (the outermost short-dashed and dashed curves always denote $\rho w = 10^{-6}$ and 10^{-5}). In the first panel, the NS located for $y < 0$ is more massive one. The filled circle near the origin in the last panel shows the region inside the apparent horizon.

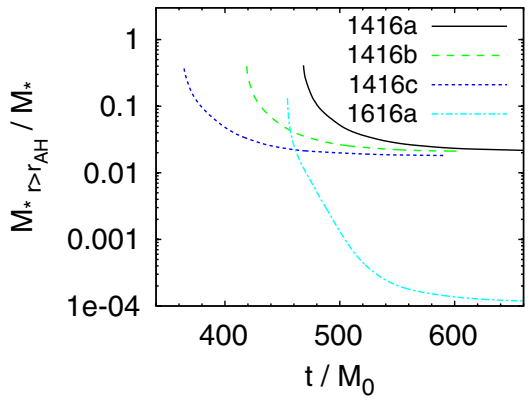

FIG. 9 (color online). Evolution of rest mass of material located outside apparent horizon for NS1416a–c, and NS1616a.

Figure 9 plots the time evolution of the total rest mass of material located outside apparent horizon. As mentioned above, it settles down to $\sim 2\%$ of the total rest mass at the end of the simulations for runs NS1416a–c, indicating that a disk of substantial mass is formed around the formed BH. The disk mass gradually decreases with time even at the end of the simulations, but the decrease time scale is much longer than the orbital period of the material. For a hypothetical value of $M_* = 3M_\odot$, the disk mass is about $0.06M_\odot$. By contrast, for run NS1616a, it decreases to $\sim 10^{-4}M_*$ implying that the disk of substantial mass is not formed. It is worth noting that the disk mass for model NS1416 is much larger than that for the case that stiff realistic EOSs are used for modeling NSs [4], for the same value of mass ratio: For the stiff EOSs used in the previous works [4], the disk mass around BH is less than $0.01M_\odot$ for mass ratio of $\gtrsim 0.9$ [4]. The possible reason for this difference is that the smaller-mass NS for the present EOS are less compact than those in the stiff EOSs, and hence, its outer part can spread outward more extensively. Because the EOS adopted here is not very realistic (in the realistic EOSs the radius depends on the mass in a much weaker manner), one should not consider at face value that a massive disk would be formed after the merger of unequal-mass NS-NS binaries.

In Table VI, we summarize quantities extracted from the apparent horizon of the formed BH. We note that the area and the ratio of circumferential lengths decrease by $\sim 5\%$ for the time duration of $150M_0$ after formation of the apparent horizon, and thus, the irreducible mass and spin of the BH are not determined within $\sim 5\%$ error in contrast to the case for BH-BH and BH-NS (see the next subsection) binaries even for the best-resolved run. Currently, the reason is not clear (a possible reason is that the spin parameter is too large and hence the radius of the apparent horizon is too small for the chosen grid resolution to resolve the BH accurately). Nevertheless, the final state of the BH is determined with an accuracy that is acceptable for quantitative discussion: For model NS1616, the final mass of the formed BH is $\approx 0.99M_0$, and the spin is ~ 0.81–0.84 irrespective of the grid resolution, grid structure, and chosen formalism. These results are also in good agreement with those in the simulation by Shibata's code. For model NS1416, the final mass of the BH is evaluated to be $\approx 0.97M_0$ and the spin is ~ 0.8–0.85. The BH mass is smaller than that for model NS1616. We understand this fact as follows: A disk is formed in this case and a part of mass and angular momentum are distributed to it.

TABLE VI. Numerical results for simulations of NS-NS binaries. We list the time at which apparent horizon is first formed ($T_{\rm AH}$), approximate final value of the irreducible mass of the apparent horizon ($M_{\rm irr}$), ratio of the polar circumferential length to the equatorial one for the apparent horizon (C_p/C_e), BH mass estimated from the equatorial circumferential length ($C_e/4\pi$), BH spin parameter estimated from C_p/C_e (a), energy and angular momentum carried away by gravitational waves (ΔE and ΔJ), and rest mass and angular momentum of disk formed around the BH ($M_{\rm disk}$ and $J_{\rm disk}$). The state of the disk was determined when we stopped the simulation (cf. Figure 9). For model NS1616, the mass and angular momentum of disk are determined only for run NS1616a.

Run	$T_{\rm AH}/M_0$	$M_{\rm irr}/M_0$	C_p/C_e	$C_e/(4\pi M_0)$	a	$\Delta E/M_0$	$\Delta J/J_0$	$M_{\rm disk}/M_0$	$J_{\rm disk}/J_0$
NS1616s	478	0.86–0.87	0.81–0.83	0.993	0.83–0.86	0.7%	12%	—	—
NS1616a	454	0.85–0.87	0.79–0.83	0.995	0.83–0.89	0.7%	11%	$\sim$0.01%	$\sim$0.03%
NS1616aF	448	0.85–0.87	0.79–0.83	0.995	0.83–0.89	0.7%	12%	—	—
NS1616b	410	0.84–0.88	0.78–0.84	0.997 ± 0.001	0.81–0.91	0.7%	11%	—	—
NS1616bF	399	0.85–0.88	0.78–0.84	0.995 ± 0.001	0.81–0.91	0.7%	11%	—	—
NS1616c	357	0.84–0.88	0.78–0.84	0.997 ± 0.002	0.81–0.91	0.6%	10%	—	—
NS1616cF	349	0.84–0.89	0.78–0.84	0.996 ± 0.001	0.81–0.91	0.6%	10%	—	—
NS1616d	386	0.84–0.89	0.78–0.84	0.995 ± 0.001	0.81–0.91	0.7%	11%	—	—
NS1616e	325	0.84–0.89	0.78–0.84	0.995 ± 0.003	0.81–0.91	0.7%	8%	—	—
Shibata	423	0.874	0.83	0.989 ± 0.001	0.83	0.8%	12%	—	—
NS1416a	469	0.83–0.85	0.80–0.85	0.971	0.80–0.88	0.5%	9%	2.4%	6.0%
NS1416b	419	0.82–0.85	0.78–0.85	0.976 ± 0.001	0.80–0.90	0.4%	8%	2.3%	5.9%
NS1416c	364	0.80–0.85	0.76–0.86	0.982 ± 0.002	0.78–0.93	0.4%	7%	2.0%	5.1%

For BHs formed after the merger of equal-mass BH-BH binaries, the final spin parameter is ≈ 0.7. For the best-resolved run, the spin parameter is 0.85 ± 0.02 for model NS1616 and 0.83 ± 0.03 for model NS1416. Thus, the spin parameter of the BHs formed after the merger of equal-mass NS-NS binary is by $\sim$0.1–0.15 larger. The primary reason for this difference is that the angular momentum carried away by gravitational waves in the merger of NS-NS binaries is much smaller than that in the merger of BH-BH binaries: For BH-BH binaries, $\sim$30% of the initial angular momentum is dissipated by gravitational radiation, whereas for NS-NS binaries, it is $\sim$10%. This difference comes primarily from difference in amplitude of gravitational waves emitted in the final merger phase. BH-BH binaries can take much closer orbital separations than NS-NS binaries can because BHs are more compact than NSs. Thus, gravitational waves of a higher amplitude are emitted at the final inspiral orbit in the former cases. In addition, ringdown gravitational waves associated with quasinormal-mode oscillation of fundamental $l = m = 2$ mode is excited more significantly in the merger phase for BH-BH binaries. Indeed, the amplitude is as high as that emitted at the last inspiral orbit (cf. Figure 4). By contrast, in the case of NS-NS binaries, it is not excited as significantly as in the case of BH-BH binaries (cf. Figure 12), because of smaller degree of nonaxisymmetric deformation of the spacetime curvature at the merger. In another paper [11], we performed simulations for NS-NS binaries using a realistic stiff EOS, which is highly different from the Γ-law EOS with $\Gamma = 2$, and found that the final spin parameter is ≈ 0.8 for the BH-formation case. Thus, the value of $\sim$0.8 for the spin parameter seems to be a universal outcome for the BHs formed after the merger of NS-NS binaries.

4. Conservation of energy and angular momentum

Validity of the results about mass and spin of BHs finally formed is checked by examining whether the following conservation relations hold:

$$M_{\rm BHf} + M_{\rm disk} + \Delta E = M_0, \tag{69}$$

$$M_{\rm BHf}^2 a + J_{\rm disk} + \Delta J = J_0. \tag{70}$$

Here, $M_{\rm disk}$ and $J_{\rm disk}$ are the rest mass and the angular momentum of disk, respectively. As in Refs. [29,30], $J_{\rm disk}$ is calculated approximately by

$$J_{\rm disk} \equiv \int_{r>r_{\rm AH}} \rho \alpha h u^t u_\varphi \sqrt{\gamma} d^3x, \tag{71}$$

where the φ coordinate is defined for an origin determined from the maximum of ρ_*, which is approximately equal to the center of the BH. For model NS1616 for which disk mass is $\sim 10^{-4} M_*$ and negligible, the energy conservation holds within a 0.2–0.3% error and the angular momentum one holds with a 2–3% error. For model NS1416, errors in the energy and angular momentum conservations are $\approx$ 0.3% and $\sim$5%, respectively. Here, the error is defined, respectively, by

$$1 - (M_{\rm BHf} + M_{\rm disk} + \Delta E)/M_0, \tag{72}$$

$$1 - (M_{\rm BHf}^2 a + J_{\rm disk} + \Delta J)/J_0. \tag{73}$$

The magnitude of the error is approximately the same as that for BH-BH binaries. For both models, the primary error source in the angular momentum conservation comes from the fact that C_p/C_e is not determined in a good accuracy.

5. Merger time

The merger time, defined as the time at formation of apparent horizon ($T_{\rm AH}$), systematically increases with improving grid resolution. Figure 10 plots $T_{\rm AH}$ as a function of h_{L-1}^2 for runs NS1616s, NS1616a–c, and NS1616aF–cF. This figure shows a systematic behavior for convergence of $T_{\rm AH}$ irrespective of the chosen formalism and spatial gauge. For models NS1416a–c, the similar relation holds, and hence, we do not present the figure. It is worth noting that runs with the $\tilde{\Gamma}^i$-BSSN and F_i-BSSN formalisms give approximately the same values of $T_{\rm AH}$. This indicates that in the absence of BHs, difference in the spatial gauge does not affect the orbital evolution of compact stars significantly. Another point to be noted is that the convergence is relatively slow, although the order of convergence appears to be second order. Extrapolating the results to the limit $h_{L-1} \to 0$ under the assumption of the second-order convergence, a realistic time of $T_{\rm AH}$ is determined to be $\approx 530 M_0$ for sequences of both formalisms. Thus, even for the best-resolved run NS1616s, the value of $T_{\rm AH}$ is underestimated by $\approx 50 M_0$ (by $\sim$10% of $T_{\rm AH}$), which is approximately a half orbital period for an innermost stable circular orbit with $M_0 \Omega \sim 0.06$ [51,53]. This indicates that for obtaining an orbital evolution and gravitational waveforms with a small phase error (say within $10 M_0$ error), the grid resolution should be by a factor of $\sim$2 finer than that in

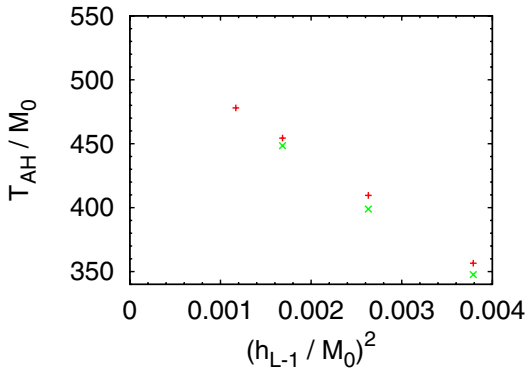

FIG. 10 (color online). $T_{\rm AH}$ as a function of h_{L-1}^2 for runs NS1616a–c and s (plus) and NS1616aF–cF (cross).

the best-resolved run in the current code, or we should employ a hydrodynamic scheme in which numerical dissipation is not as large as that in the present code (but see discussion related to gravitational waves described below).

The Taylor T4 formalism predicts the approximate merger time as $650M_0$, which is obtained by integrating Eq. (50) from the orbit of $\Omega = \Omega_0$ to the orbit of $M_0\Omega = 0.1$ at which the merger should already proceed. This value is much larger than the extrapolated numerical result for the merger time. We explain this discrepancy as follows: In the Taylor T4 formalism, effects due to tidal deformation of the NSs are not included. The tidal-deformation effect increases attraction force between two NSs, and as a result, the inspiral phase is significantly shortened [54], in particular, for orbits with $M_0\Omega \gtrsim 0.04$. Indeed, numerical study for quasi-equilibrium NS-NS binaries indicates that tidal effect plays an important role for $M_0\Omega \gtrsim 0.04$ (e.g., [51,53]). Thus, it is natural that the Taylor T4 formalism significantly overestimates the merger time.

6. Rest-mass conservation

Figure 11 plots the change in total rest mass with time for runs NS1616a–d and NS1616s. (Similar relations also hold for runs NS1416a–c; e.g., the maximum violation of the rest-mass conservation is $\approx 1.5\%$ for run NS1416a.) Although the total rest mass should be conserved, this is not guaranteed in our AMR code (note that in Shibata's code in which unigrid is employed, the rest mass is conserved in a much better accuracy). The reasons for this are as follows: (i) Numerical flux determined at refinement boundaries of a child level does not exactly agree with that determined for the corresponding parent level. This mismatch of the flux generates slight violation of the rest-mass conservation. (ii) At the moment of the regridding, values for a part of the child level are given by interpolating the values of its corresponding parent level. This process does not guarantee the rest-mass conservation. However, Fig. 11

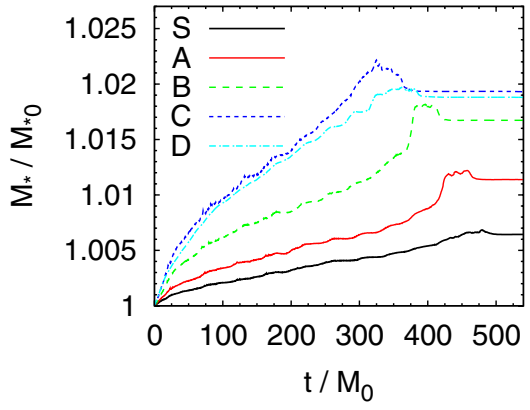

FIG. 11 (color online). Change in total rest mass due to numerical error with time for runs NS1616s (thick solid curve), NS1616a (solid curve), NS1616b (long-dashed curve), NS1616c (dashed curve), and NS1616d (dotted-dashed curve).

shows that the magnitude of violation is small. For the best-resolved runs NS1616s, the violation is at most 0.7%, and furthermore, the magnitude of the violation systematically converges with improving the grid resolution. (The value of $|M_*/M_{*0} - 1|$ converges approximately at second order.) Therefore, we conclude that in the well-resolved simulations, the violation of the rest-mass conservation only gives a minor effect for the numerical results.

7. Gravitational waves

Figures 12(a) and 12(b) plot gravitational waveforms for runs NS1616s and NS1416a, respectively. In the early phase with $t_{\rm ret} \lesssim 400M_0$, the waveforms are characterized by the inspiral waveforms, and in the final phase, ringdown gravitational waveforms associated with a quasinormal mode of the formed BH are seen. In these simulations, the BH is not immediately formed at the onset of merger because thermal energy generated by shock heating and/or centrifugal force due to large angular momentum halt the collapse of the merged object to a BH for a short time scale. The transient object emits quasiperiodic gravitational waveforms just before gravitational waves associated with a quasinormal mode are emitted. Amplitude of gravitational waves associated with the quasiperiodic oscillation and the quasinormal mode is by about 1 order of magnitude smaller than that emitted in the final inspiral phase. This feature is different from that in the merger of BH-BH binaries. Because of this small amplitude, total energy and angular momentum carried away by gravitational waves are much smaller than those in the merger of BH-BH binaries (see Table VI). Because of the relatively small emitted angular momentum, the spin parameter of the BH finally formed is by a factor of 0.1–0.15 larger than that in the merger of BH-BH binaries, as already mentioned.

Figure 12(c) compares gravitational waveforms (plus mode) for run NS1616a and run by Shibata's code. It is seen that two results agree qualitatively well besides a phase error caused by the difference in the grid resolution. This shows that the results by SACRA and Shibata's code agree in a reasonable manner. Figure 12(d) compares gravitational waveforms (plus mode) for runs NS1616s, a, and b. For comparing gravitational waveforms for the last inspiral and merger phases, the data for NS1616a and NS1616b are plotted as functions of $t_{\rm ret} + 10M_0$ and $t_{\rm ret} + 54M_0$ for $h_+ \cos(0.2\pi) - h_\times \sin(0.2\pi)$ and $-[h_+ \cos(0.2\pi) - h_\times \sin(0.2\pi)]$, respectively. It is found that the waveforms in the late $\sim$2 inspiral orbits (about for 3–4 wavelengths) agree well among three models. From the orbit just before the merger, the difference in the wave phases becomes outstanding. This is because the evolution in such a phase depends sensitively on the degree of tidal deformation, which is sensitive to the grid resolution. The agreement of the waveforms in the intermediate phase also indicates that the strong dependence of $T_{\rm AH}$ on the grid resolution is primarily due to the fact that the inspiral orbit

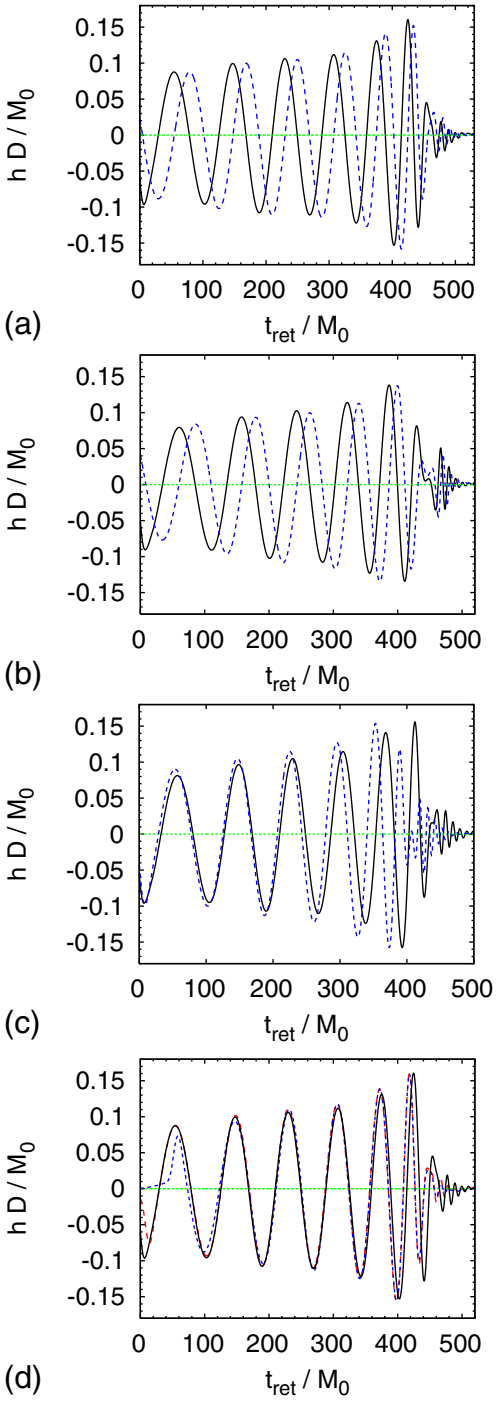

FIG. 12 (color online). (a) Gravitational waveforms for run NS1616s. $l = m = 2$ mode is plotted. The solid and dashed curves denote the plus and cross modes, respectively. (b) The same as (a) but for run NS1416a. (c) h_+ for run NS1616a (solid curve) and run by Shibata's unigrid code (dashed curve). (d) h_+ for runs NS1616s, a, and b (solid, long-dashed, and dashed curves). For runs NS1616a and NS1616b, the gravitational waveforms are plotted as functions of $t_{\rm ret} + 10M_0$ and $t_{\rm ret} + 54M_0$, respectively. In addition, for NS1616a and b, $h_+ \cos(0.2\pi) - h_\times \sin(0.2\pi)$ and $-[h_+ \cos(0.2\pi) - h_\times \sin(0.2\pi)]$ are plotted to align the phase.

at a large orbital separation depends on the grid resolution. Thus, to follow at least only the late $\sim$2 orbits, the grid resolution used in the present work is acceptable.

Figure 13 plots angular velocity of gravitational waves as a function of time for runs NS1616a–c. The angular velocity (and frequency) of gravitational waves gradually increases in the inspiral phase. Then, at the onset of merger, it forms a spiky peak. This appears simply due to the fact that the amplitude of gravitational waves remains approximately a constant for a moment soon after merger sets in, and the denominator of Eq. (64) approaches to zero. In such moment, collapse of the merged object to a BH is halted for a short time scale and a very compact object of a relatively small nonsphericity is temporally formed. However, this phase is short and the compact object soon collapses to a BH. Then, gravitational waves associated with a quasinormal mode are emitted, and therefore, the angular velocity eventually reaches $M_0\Omega \approx 0.3$. This value agrees approximately with the angular velocity of the fundamental $l = m = 2$ quasinormal mode of a BH with spin parameter $\sim$0.8 and the final ADM mass $\sim M_0$.

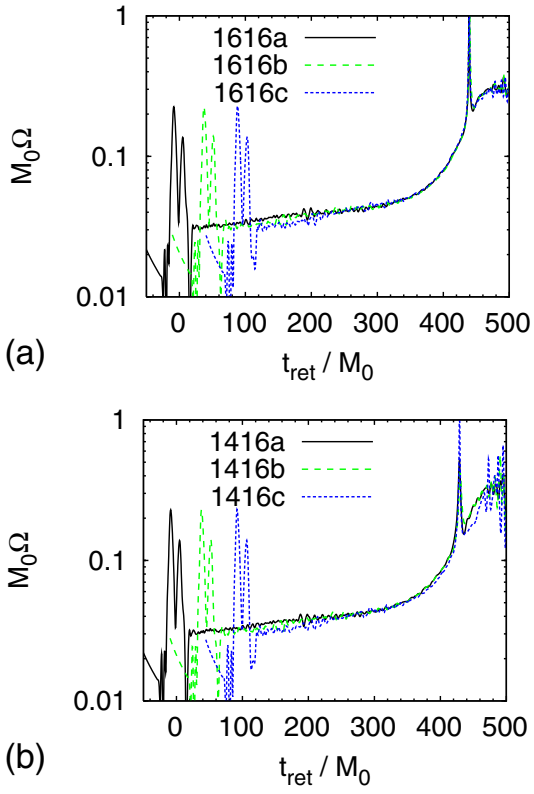

FIG. 13 (color online). (a) Angular velocity of gravitational waves as a function of retarded time for runs NS1616a–c. For runs NS1616b and NS1616c, the curves are plotted as functions of $t_{\rm ret} + 46M_0$ and $t_{\rm ret} + 97M_0$, respectively. (b) The same as (a) but for runs NS1416a–c. For runs NS1416b and NS1416c, the curves are plotted as functions of $t_{\rm ret} + 47M_0$ and $t_{\rm ret} + 101M_0$, respectively.

Figure 13 also indicates slow convergence of the merger time with improving the grid resolution; for improving the grid resolutions, the inspiral time increases by a large factor. This makes us reconfirm that for an accurate long-term simulation of inspiraling NS-NS binaries, a high grid resolution is required. However, this figure also shows that for $t_{\rm ret} \gtrsim 200M_0$, the curves for runs NS1616a and NS1616b and for runs NS1416a and NS1416b approximately agree with each other. This reconfirms that for computing gravitational waveforms for the late $\sim$2 orbits, the grid resolution for NS1616a and NS1416a is acceptable.

Gravitational waveforms for model NS1416 are very similar to those for model NS1616. One difference worth noting is that energy and angular momentum carried away by gravitational waves for model NS1416 are smaller than those for model NS1616. The reason for these small values is that tidal disruption occurs at a relatively large orbital separation. For the case of NS-NS binaries, gravitational waves are emitted most effectively at the final inspiral phase just before the merger. Thus, absence of such phase due to the tidal disruption significantly decreases the total amount of gravitational wave emission.

C. BH-NS binaries

As the last test, we performed simulations for BH-NS binaries.

1. Initial condition

We adopt BH-NS binaries in quasi-equilibrium circular orbits computed in the moving puncture framework as initial conditions, following our previous works [29,30] (see these references for basic equations and methods for solving them). We pick up two models in this work. In both models, the BH is nonspinning and the NS has the irrotational velocity field with its compactness ≈ 0.145. Ratio of irreducible mass of the BH to gravitational mass of the NS in isolation is $\approx$ 3.05–3.06. Several key quantities are listed in Table VII. Model BHNS-A is the same as model A of Ref. [30] in which the initial value of the angular velocity satisfies $M_0\Omega_0 \approx 0.040$. In the previous paper [29], we find that for the best-resolved run, the binary orbits for about 1.7 times before the onset of tidal disruption for this model. We compare numerical results obtained by SACRA with those in the previous simulation. The other model, referred to as BHNS-B, has a smaller initial orbital angular velocity as $M_0\Omega_0 \approx 0.034$. Third post-Newtonian equations of motion for two point masses predict that the binary orbits $\sim$4 times before the onset of merger. We will show that our code can stably and accurately follow such a long-term orbit.

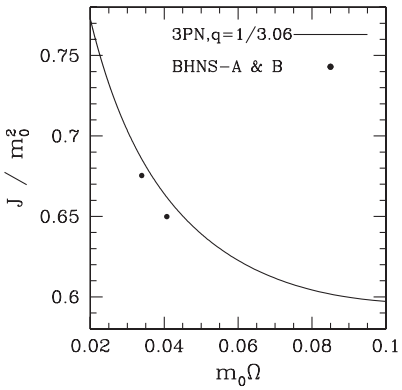

FIG. 14. Angular momentum (J/m_0^2) vs angular velocity ($m_0\Omega$) for models BHNS-A and B. For comparison, the same relation for a binary of $q = 1/3.06$ in the third post-Newtonian theory (the solid curve) is shown together.

As we indicated in the previous paper [30], the quasi-equilibria used in this paper have a nonzero eccentricity (see Ref. [55] for the related topic). The primary reason seems to be a slight deficit of angular momentum in the quasi-equilibria. Figure 14 plots angular momentum (J/m_0^2) as a function of angular velocity ($m_0\Omega$) for models BHNS-A and B as well as that calculated for two point particles in the third post-Newtonian theory [2]. This shows that the angular momenta for models BHNS-A and B are by $\sim$1% smaller than those in the third post-Newtonian results for a given value of $m_0\Omega$. Because of this deficit, the orbital separation quickly decreases soon after the simulations are started. More detailed analysis of the quasi-equilibria in the moving puncture framework as well as comparison of the results with those in the excision framework [56–58] will be presented in a separate paper [59].

2. Setting

Following previous papers [29,30], the initial condition for α is modified from the solution of the quasi-equilibrium

TABLE VII. List of several quantities for quasicircular states of BH-NS binaries. We show the mass parameter of puncture ($M_{\rm p}$), irreducible mass of the BH ($M_{\rm BH}$), rest mass of the NS (M_*), mass ($M_{\rm NS}$) and compactness defined by ratio of $M_{\rm NS}$ to circumferential radius ($R_{\rm NS}$) of the NS in isolation, mass ratio ($q = M_{\rm NS}/M_{\rm BH}$), ADM mass at $t = 0$ (M_0), total angular momentum at $t = 0$ in units of M_0 (J_0/M_0^2), and $M_0\Omega_0(m_0\Omega_0)$ where Ω_0 is orbital angular velocity at $t = 0$ and $m_0 = M_{\rm BH} + M_{\rm NS}$. The BH irreducible mass is computed from the area of apparent horizon A as $(A/16\pi)^{1/2}$. All these quantities are normalized by κ appropriately to be dimensionless.

Model	$M_{\rm p}$	$M_{\rm BH}$	M_*	$M_{\rm NS}$	$M_{\rm NS}/R_{\rm NS}$	q	M_0	J_0/M_0^2	$M_0\Omega_0(m_0\Omega_0)$
BHNS-A	0.4185	0.4260	0.1500	0.1395	0.145	0.327	0.5604	0.662	0.0403 (0.0408)
BHNS-B	0.4185	0.4250	0.1500	0.1395	0.145	0.328	0.5598	0.687	0.0337 (0.0340)

TABLE VIII. The same as Table V but for simulations of models BHNS-A and BHNS-B. Δx is the minimum grid spacing, $R_{\rm diam}$ the coordinate length of semi-major diameter of the NS, L the location of outer boundaries along each axis, λ_0 the gravitational wavelength at $t = 0$, and $\Delta x_{\rm gw}$ the grid spacing at which gravitational waves are extracted. $M_{\rm p}$ denotes the mass parameter of puncture BH [30].

Run	Levels	N	$\Delta x/M_0(\Delta x/M_{\rm p})$	$R_{\rm diam}/\Delta x$	$L/M_0(L/\lambda_0)$	$\Delta x_{\rm gw}/M_0$
BHNS-A1, A1F	8 (4 + 4)	30	0.036 (0.048)	76	138 (1.8)	0.58–2.32
BHNS-A2, A2F	8 (4 + 4)	24	0.045 (0.060)	62	138 (1.8)	0.72–2.88
BHNS-A3, A3F	8 (4 + 4)	20	0.054 (0.072)	51	138 (1.8)	0.86–3.46
Ref. [30]	—	—	0.047 (0.063)	59	66.7 (0.86)	1.05
BHNS-B1	8 (4 + 4)	30	0.036 (0.048)	76	138 (1.5)	0.58–2.32
BHNS-B2	8 (4 + 4)	24	0.045 (0.060)	61	138 (1.5)	0.72–2.88
BHNS-B3	8 (4 + 4)	20	0.054 (0.072)	51	138 (1.5)	0.86–3.46

state so as to satisfy the condition of $\alpha > 0$ everywhere. For the shift, we adopt the quasi-equilibrium solution with no change.

Simulations were performed for three grid resolutions (see Table VIII). For all the cases, a numerical domain is composed of eight refinement levels (four finer and coarser levels) and locations of outer and refinement boundaries are chosen to be the same. The NSs are covered by the finest and second-finest levels. The finest grid resolution for run BHNS-A2 is approximately the same as that for run A0 in Ref. [30]. The $\tilde{\Gamma}^i$-BSSN formalism is used for all the runs performed in the AMR code, and the F_i-BSSN formalism is used for the simulations of model BHNS-A1. In the following, results with the $\tilde{\Gamma}^i$-BSSN formalism are basically presented, because they depend very weakly on the chosen formalism, as in the case of NS-NS binaries.

3. Evolution of the BH and the NS, and final outcome

Figure 15(a) plots orbital trajectories of the NS for model BHNS-A. Figures 15(b) and 15(c) plot $x^i_{\rm NS} - x^i_{\rm BH}$ for models BHNS-A and BHNS-B, respectively. For the best-resolved run, orbital trajectory of the BH is also plotted in Fig. 15(a). Here, the trajectories of the NSs are determined from the location of the maximum value of ρ_*, and that of the BHs is from the location of the moving puncture. For both models BHNS-A and BHNS-B, the NS is tidally disrupted by the companion BH before it is swallowed by the BH. Before the onset of tidal disruption, models BHNS-A and BHNS-B spend about 2 and about $3 + 3/4$ orbits, respectively, for the best-resolved runs. Here, the approximate time for the onset of tidal disruption (referred to as $T_{\rm disr}$) is determined from the time at which 1% of the total rest mass is swallowed into apparent horizon of the BH.

For runs BHNS-A1, A2, and A3, the tidal disruption starts at ~1.95, 1.75, and 1.45 orbits, respectively, (see also Table IX for the time in units of M_0). In the run A0 of Ref. [30], the tidal disruption starts approximately at the same time as that for run BHNS-A2. This is quite reasonable because the grid resolution around the BH and the NS for run BHNS-A2 agrees approximately with that of run A0 of Ref. [30]. The values of $T_{\rm disr}$ depend weakly on the chosen formalism for a given grid resolution. This illustrates that the numerical results depend weakly on the formalism and gauge.

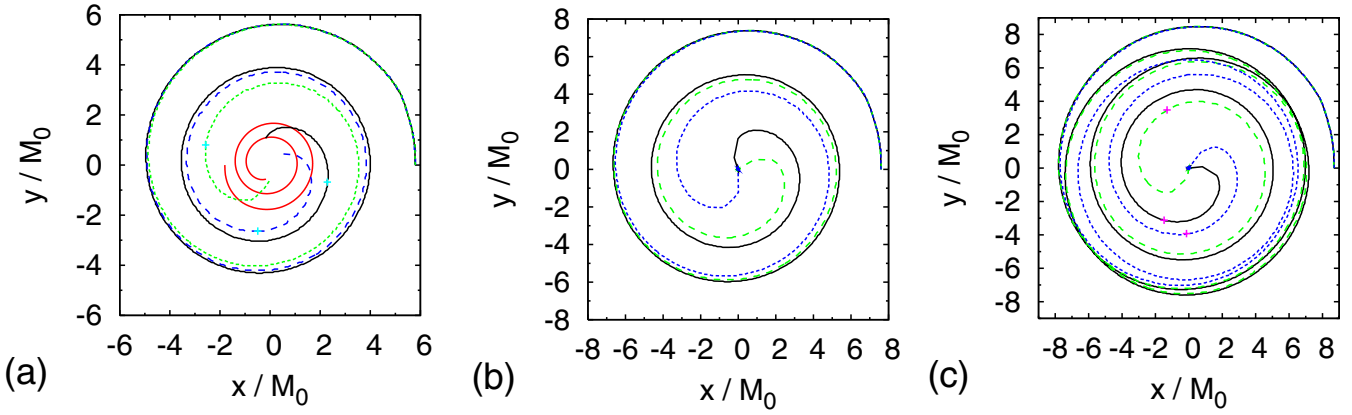

FIG. 15 (color online). (a) Orbital trajectories of NSs for runs BHNS-A1 (solid curve), BHNS-A2 (long-dashed curve), and BHNS-A3 (dashed curve). Trajectory of the BH for run BHNS-A1 (inner solid curve) is also plotted. (b) The same as (a) but for $x^i_{\rm NS} - x^i_{\rm BH}$. (c) The same as (b) but for runs BHNS-B1 (solid curve), BHNS-B2 (long-dashed curve), and BHNS-B3 (dashed curve). For (a) and (c), the plus mark denotes location of the NSs at the onset of tidal disruption (at $t = T_{\rm disr}$).

TABLE IX. Numerical results for simulations of BH-NS binaries. We list the approximate time at the onset of tidal disruption ($T_{\rm disr}$), irreducible mass of apparent horizon formed after merger ($M_{\rm irr}$), ratio of polar circumferential length to the equatorial one for the apparent horizon formed after merger (C_p/C_e), final BH mass estimated from the equatorial circumferential length ($C_e/4\pi$), final BH mass estimated from $M_{\rm irr}$ and C_p/C_e ($M_{\rm BHf}$), final spin parameter of the BH estimated from C_p/C_e, and energy (ΔE) and angular momentum (ΔJ) carried away by gravitational waves.

Run	$T_{\rm disr}/M_0$	$M_{\rm irr}/M_0$	C_p/C_e	$C_e/(4\pi M_0)$	$M_{\rm BHf}/M_0$	a	$\Delta E/M_0$	$\Delta J/J_0$
BHNS-A1	206	0.942	0.938	0.982	0.983	0.55	0.9%	14%
BHNS-A1F	202	0.942	0.938	0.983	0.983	0.55	0.9%	14%
BHNS-A2	186	0.942	0.938	0.983	0.983	0.55	0.8%	12%
BHNS-A2F	182	0.943	0.939	0.983	0.984	0.55	0.8%	13%
BHNS-A3	158	0.943	0.935	0.985	0.986	0.56	0.7%	11%
BHNS-A3F	156	0.945	0.937	0.986	0.987	0.55	0.7%	11%
Ref. [30]	179	0.935	0.939	0.975	0.976	0.55	0.7%	11%
BHNS-B1	472	0.940	0.937	0.982	0.982	0.56	0.9%	17%
BHNS-B2	433	0.940	0.936	0.983	0.983	0.56	0.8%	15%
BHNS-B3	353	0.941	0.933	0.985	0.985	0.57	0.8%	15%

For runs BHNS-B1, B2, and B3, the tidal disruption starts at $\sim$3.7, 3.3, and 2.75 orbits, respectively. Because the time spent in the inspiral phase for model BHNS-B is longer than that for model BHNS-A, numerical error is accumulated more, resulting in a larger dispersion in $T_{\rm disr}$. A characteristic feature for model BHNS-B is that its orbital eccentricity is initially very large: Soon after the simulation is started, the orbital separation decreases by a large factor, and then, it significantly increases. The first two orbit are obviously different from circular orbits. Gravitational waveforms shown later also illustrate that the orbit is eccentric. As mentioned in Sec. IV C 1, the primary reason for the presence of the eccentricity is that the angular momentum of the quasi-equilibrium initially given is likely to be by $\sim$1% smaller than that for the true quasi-equilibrium. However, in the last $\sim$2 orbits, the orbital separation gradually and monotonically decreases to merger (see the trajectory for run BHNS-B1), suggesting that the eccentricity is reduced by emission of gravitational waves.

As reported above, the time at the onset of tidal disruption $T_{\rm disr}$ systematically increases with improving the grid resolution. Figures 16(a) and 16(b) plot $T_{\rm disr}$ as a function of h_{L-1}^2 for models BHNS-A and BHNS-B, respectively. Figure 16(a) shows that $T_{\rm disr}$ is approximately proportional to h_{L-1}^2. Extrapolating this relation to $h_{L-1} \to 0$, it is found that the converged value for $T_{\rm disp}$ is $\approx 240M_0$. This suggests that by the onset of tidal disruption, the binary would orbit for $\sim 9/4$ times. Thus, the results in run BHNS-A1 are near the convergent ones, although the phase error of $\approx 30M_0$ (about a quarter orbit) would still be present. The value determined by the extrapolation is much smaller than the value predicted by the Taylor T4 formalism, which gives $\approx 315M_0$. This is reasonable because the Taylor T4 formalism neglects effects associated with tidal deformation of the NS and BH, which accelerates the inward motion and shortens $T_{\rm disr}$ (e.g., see Ref. [54]).

Figure 16(b) shows that the results of $T_{\rm disr}$ converge with improvement of the grid resolution at an order better than the second order. The results for three grid resolutions appear to be approximately fourth-order convergent, but such a high order is unlikely for the chosen scheme for hydrodynamics. This may be due to a too small value of $T_{\rm disr}$ for run BHNS-B3 for which convergence may not

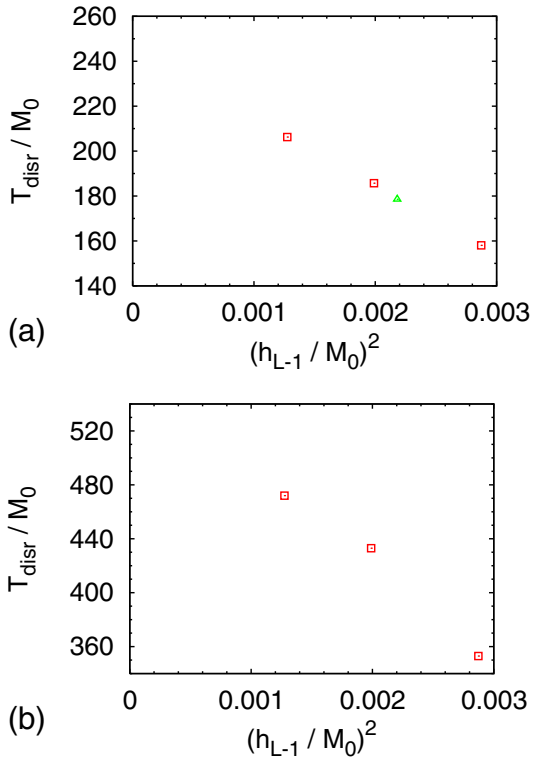

FIG. 16 (color online). $T_{\rm disr}$ as a function of h_{L-1}^2. (a) The open squares denote the data by runs BHNS-A1–A3, and the triangle denotes the result obtained in Ref. [30]. (b) The same as (a) but for the data by runs BHNS-B1–B3.

hold. Thus, we assume the second-order convergence, as inferred from the result for model BHNS-A, and use the values for runs BHNS-B1 and B2 for extrapolation. Then, the extrapolation gives $T_{\rm disr} \approx 540M_0$. Thus, in run BHNS-B1, the value of $T_{\rm disr}$ is underestimated by $\approx 70M_0$. (Note that if we assume the fourth-order convergence, the predicted value of $T_{\rm disr}$ is $\approx 500M_0$.) The primary reason for this underestimation is that numerical dissipation spuriously shortens the inspiral time. The extrapolated value of $T_{\rm disr} \approx 540M_0$ is again smaller than the value predicted by the Taylor T4 formalism, which gives $\approx 585M_0$. As mentioned above, this disagreement is reasonable because tidal effects are neglected in the Taylor T4 formalism.

Figure 17 plots the evolution of $M_{\rm irr}/M_0$, C_p/C_e, and $C_e/(4\pi M_0)$ as functions of time. This shows that BHs are approximately in stationary states before and after tidal disruption of the companion NS. By contrast, they quickly evolve during tidal disruption and subsequent accretion process, irrespective of the initial condition. The figure for C_p/C_e shows that the BH is approximately nonrotating before the onset of tidal disruption because it is approximately unity. However, as the mass accretion proceeds, its value decreases, reflecting the fact that the BH spins up by getting angular momentum from the infalling material. The mass accretion is also reflected in the figures of $M_{\rm irr}/M_0$ and $C_e/4\pi M_0$ because they increase after the onset of tidal disruption. The values of these quantities are approximately the same before the onset of tidal disruption, reflecting that the spin of the BH is approximately zero. After the onset of tidal disruption, these are different, because the final state is a spinning BH for which $M_{\rm irr} \neq C_e/4\pi$.

The final values of $M_{\rm irr}$, C_p/C_e, and $C_e/(4\pi M_0)$ for both models BHNS-A and BHNS-B depend only weakly on the grid resolution. In particular, the results for models BHNS-A1 and BHNS-A2 and for BHNS-B1 and BHNS-B2 show approximate convergence. This indicates that with the present numerical simulation, the final state of the BH is determined with good accuracy, although the merger time depends strongly on the grid resolution.

The final value of the BH spin for model BHNS-A agrees approximately with the result in Ref. [30]. As reported in Ref. [30], the final value of the BH spin is smaller than the initial spin of the system. The reason is that gravitational waves carry away a substantial fraction of angular momentum. (For the previous result in Ref. [30], a part of the angular momentum is distributed to disk, and this is also a part of the reason.) The final value of the BH mass for model BHNS-A slightly disagrees with the previous result [30]. The reason for this difference is that a disk of $\sim 0.017M_0$ is formed around the BH in the previous result (see discussion in Sec. IV C 5).

4. Conservation of energy and angular momentum

The numerical results for the final outcome are checked by examining whether or not the conservation relations Eqs. (69) and (70) hold. As shown below, the contribution of disk formed around the BH is negligible in this case. From Table IX, we find that errors in the conservation for the best-resolved runs are $\approx 1\%$ for the energy and $\approx 5\%$ for the angular momentum; $1 - \Delta E/M_0 \approx 1\%$ and $1 - \Delta J/J_0 \approx 5\%$. Namely, the final values of mass and angular momentum of the BH are smaller than those expected from

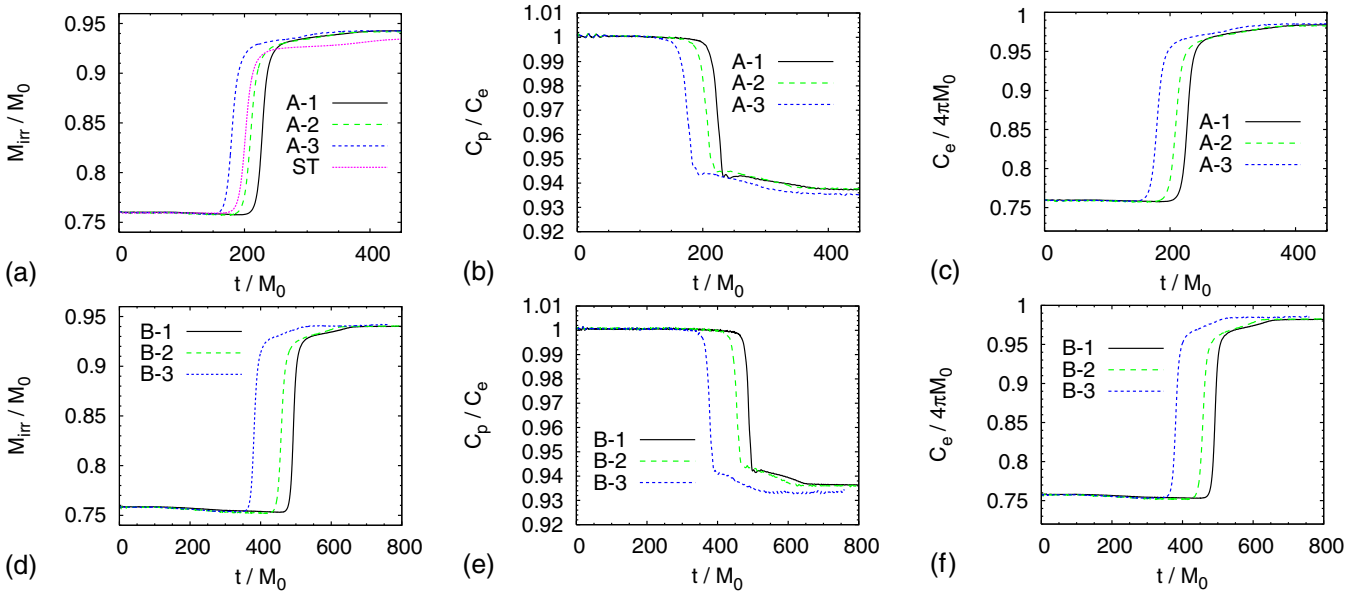

FIG. 17 (color online). (a) $M_{\rm irr}$ of the BH as a function of time for runs BHNS-A1–A3. "ST" denotes the results of run A0 in Ref. [30]. (b) The same as (a) but for C_p/C_e. (c) The same as (a) but for $C_e/(4\pi M_0)$. (d) The same as (a) but for BHNS-B1–B3. (e) The same as (d) but for C_p/C_e. (f) The same as (d) but for $C_e/(4\pi M_0)$.

the conservation relation. The possible reasons are either (i) the energy and angular momentum carried away by gravitational radiation might be underestimated or (ii) during the evolution, the energy and angular momentum might be dissipated by some spurious numerical effects. We note that the conservation relations hold in a much better manner in the previous result [30] (in this case, contribution of disk plays an important role). Thus, the reason for the violation of conservation may be associated with interpolation and extrapolation performed in the AMR algorithm, which are absent in the previous simulation [30]. Currently, the source for the error is not specified. Improving the accuracy for the conservation is an issue for the future work.

5. Disk mass

Figure 18 displays snapshots of density contour curves and density contrasts as well as the location of the BH, from tidal-disruption phase to the semifinal state of the BH for run BHNS-B1. The tidal disruption sets in when the coordinate separation between BH and NS centers becomes $\sim 5M_0$ (see the first panel of Fig. 18). Because the separation is small and the orbit is close to the innermost stable circular orbit, the radial approaching velocity induced by gravitational radiation reaction is not small at the onset of tidal disruption. This implies that the NS is disrupted while it is approaching the BH at a high speed, which is a substantial fraction of the orbital velocity. Because of this large approaching velocity, most of the NS material is swallowed by the BH soon after the onset of tidal disruption. However, the material in the outer part of the NS still spreads outward and subsequently forms a spiral arm around the BH (see the second and third panels). Mass of the spiral arm is $\sim 0.1M_*$ initially and the spiral arm spreads to a large radius with $r \gtrsim 5M_0$ (see the third panel). These properties are qualitatively the same as those found in the previous paper [30]. However, most of the material in the spiral arm subsequently falls toward the BH and only a tiny fraction of the material can escape from the BH (see the fourth panels of Fig. 18). This result disagrees with the previous one for a given NS radius and mass ratio [30,60].

The present result indicates that the material in the spiral arm does not obtain specific angular momentum large enough for forming a disk around the BH. Although the material in the outer part receives angular momentum from the material in the inner part during tidal disruption and subsequent spiral-arm formation via an angular-momentum transport process, this effect may not play a significant role. Alternatively, some mechanisms for dis-

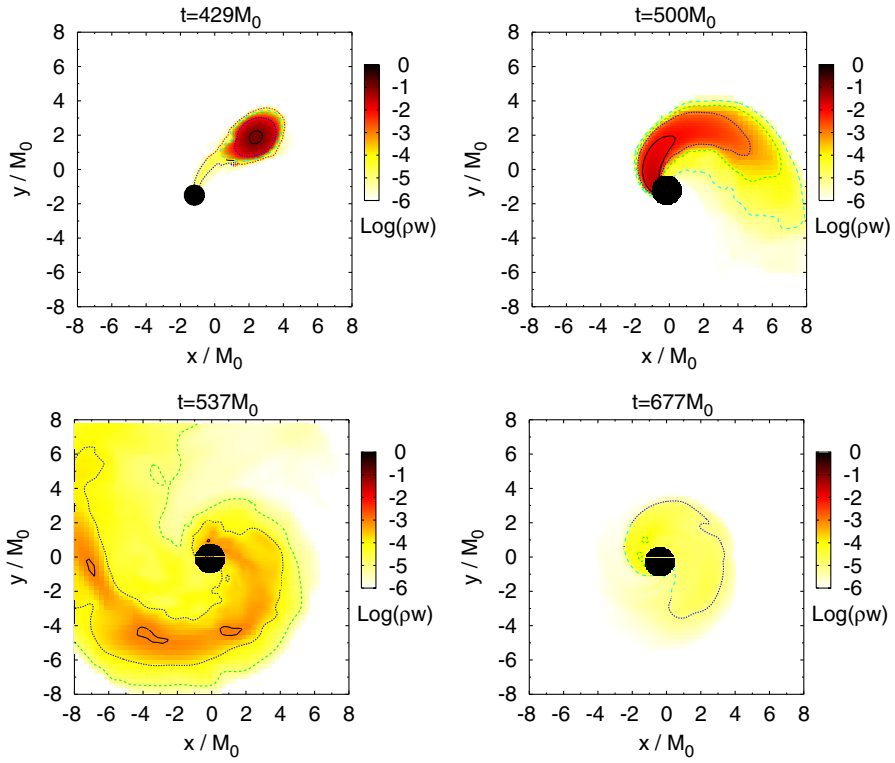

FIG. 18 (color online). Snapshots of density contour curves and density contrasts as well as location of the BH, from the onset of tidal disruption to the semifinal state of the BH for run BHNS-B1. The contour curves are plotted for $\rho w = 10^{-i}$, where $i = 2, 3, \cdots, 6$ (the outermost curve always denotes $\rho w = 10^{-6}$). The first panel denotes the state at about 3.2 orbits. The filled circles show the region inside apparent horizon.

sipation and/or anti transportation of the angular momentum may work during the evolution of the spiral arm, which might not be accurately computed in the previous work [30] due to some computational problems. For example, (i) the grid structure might not be appropriate for accurately following the angular momentum transport and (ii) in the previous simulation [30], we evolved ϕ (instead of W), which has large magnitude and gradient near the moving puncture, and hence, the trajectory of the BH, which depends sensitively on ϕ, might not be accurately computed to follow the BH orbit after the tidal disruption sets in (e.g., see Fig. 4 of Ref. [61]). For example, if the BH spuriously moves away from the spiral arm, disk formation would be spuriously enhanced. A completely alternative possibility is that the grid resolution far from the BH may not be high enough in the present grid structure to follow the evolution of the spiral arm accurately (see discussion below).

For a more specific discussion about the fate of material after the tidal disruption, we generate Figs. 19(a) and 19(b), which plot the total rest mass of material located outside apparent horizon as a function of time for runs BHNS-A1–A3 and BHNS-B1–B3, respectively. Irrespective of models and grid resolutions, this decreases monotonically after the tidal disruption sets in. However, there are two phases after the tidal disruption. For the first 100–$150M_0$, the infall rate of the material into the BH is relatively low. In such a phase, a part of the tidally disrupted material spreads outward and subsequently a spiral arm is formed around the BH (cf. the third panel of Fig. 18). The presence of this phase agrees qualitatively with our previous result [30]. In the second phase, the infall rate increases and the fraction of the rest mass around the BH decreases quickly to be much smaller than 1%, implying that a disk or torus with substantial mass is not formed. The presence of this later phase disagrees with our previous result [30,60].

A possible reason for the small disk mass is that in the present simulation, the grid resolution for following the formation of disk or torus around the BH might not be sufficient: During tidal disruption, the NS is elongated and then a fraction of material escapes from the finest-refinement domain. The motion of such material around the BH might not be accurately computed in relatively coarser levels. As a consequence, spurious dissipation or transportation of the angular momentum by numerical viscosity would happen, and the material might subsequently fall into the BH spuriously. To improve this situation, it is necessary to prepare a fine grid that covers a larger region around the BH (say within a radius of $\sim 10M_0$). To perform such simulation, modification of the present AMR scheme may be necessary, e.g., to increase the grid number N for the finer refinement levels while fixing it for the coarser levels. Such improvement is an issue for the future.

Assume that the present result for no disk formation is correct. Then, the typical life time of the accreting material

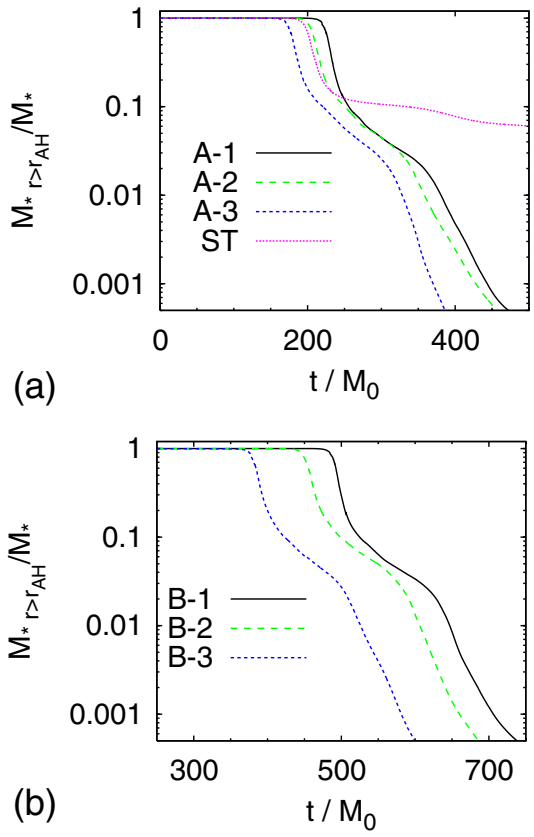

FIG. 19 (color online). Total rest mass of material located outside apparent horizon as a function of time (a) for model BHNS-A and (b) for model BHNS-B. "ST" in panel (a) denotes the result of Ref. [30].

with mass larger than $10^{-2}M_* \sim 0.01M_\odot$ is $\sim 100M_0 \approx 2.5(M_0/5M_\odot)$ ms. Here, we assume that a hypothetical mass of the NS is $\sim 1.4M_\odot$ and as a result $M_0 \sim 5M_\odot$. Such short life time is not appropriate for explaining generation of gamma-ray bursts from the accretion disk, for which the duration is longer than at least 10 ms.

6. Gravitational waves

Figure 20 plots gravitational waveforms for runs BHNS-A1 and BHNS-B1. As shown in Ref. [30], the waveforms are composed of two components. One is the inspiral waveform, and the other is the merger waveform. The amplitude quickly decreases after the onset of tidal disruption. The reason for this behavior is explained as follows: At the tidal disruption, material of the NS spreads, and then, the matter density as well as degree of nonaxial symmetry quickly decrease. Hence, the amplitude of gravitational waves, which depends strongly on the compactness and degree of nonaxial symmetry, damps. In the final phase, the ringdown gravitational waveform associated with quasinormal mode oscillation is seen. As pointed out in Ref. [30], the amplitude is not as large as that in the merger of BH-BH binaries; the amplitude is $\sim 10\%$ of

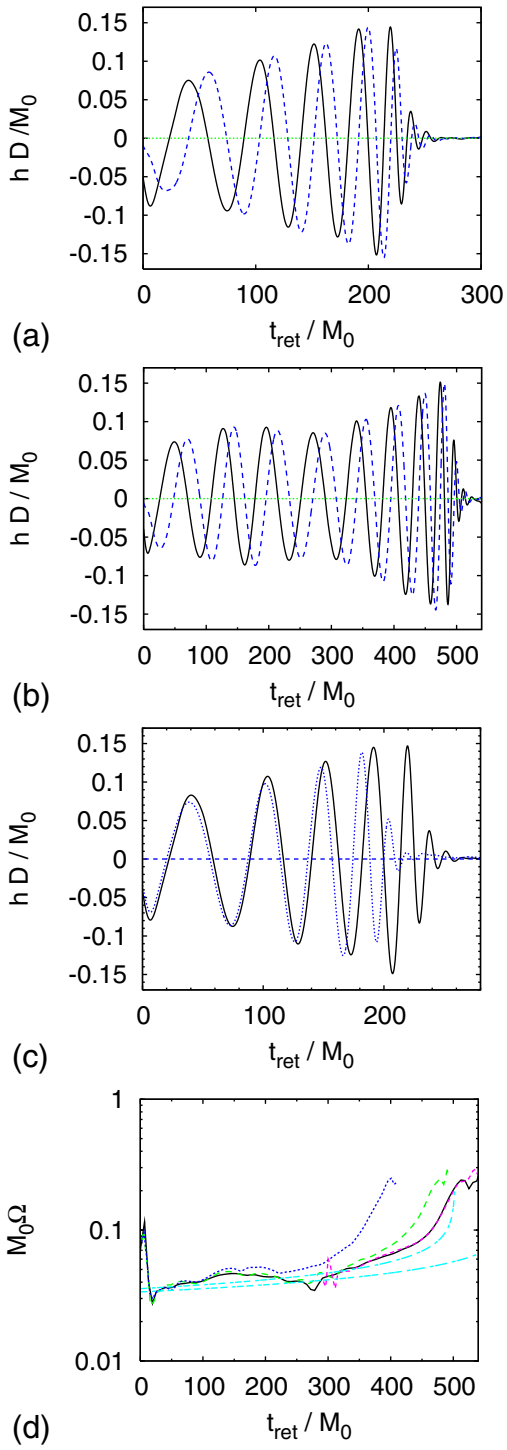

FIG. 20 (color online). Gravitational waveforms (a) for run BHNS-A1 and (b) for run BHNS-B1. The solid and dashed curves denote the plus and cross modes, respectively. (c) Plus mode of gravitational waveforms for run BHNS-A1 (solid curve) and for run A0 in Ref. [30] (dashed curve). (d) Angular velocity of gravitational waves for BHNS-B1–B3 (solid, long-dashed, dotted curves) and BHNS-A1 (dashed curve). For BHNS-A1, the curve is plotted as a function of $t_{\rm ret} + 266M_0$. The dotted-dashed curves denote the results predicted by the Taylor T4 formalism for $m_0\Omega_0 = 0.0340$ (lower curve) and 0.0360 (upper curve).

that at the last inspiral orbit. We explain the reason as follows: The material does not coherently fall into the BH because of tidal disruption, and the resulting phase cancellation suppresses coherent excitation of the quasinormal mode oscillation.

Because of a large eccentricity of the binary orbit for model BHNS-B, the gravitational waveforms are modulated in the early inspiral phase. To derive more realistic waveforms emitted during quasicircular orbits, it is necessary to prepare a better initial condition. This issue is left for future work. However, in the last $\sim$2 inspiral orbits, the BH and the NS for run BHNS-B1 appear to be approximately in a circular orbit. Thus, even if a simulation is started from an eccentric orbit, the orbit is eventually circularized. To pay attention only to gravitational waves emitted from the final inspiral to the merger phases, the present initial condition may be acceptable.

Figure 20(c) compares the plus mode of gravitational waveform for run BHNS-A1 with that of run A0 in Ref. [30]. Because the tidal disruption time ($T_{\rm disr}$) is different between two simulations, the phase does not agree. However, the qualitative feature is very similar; in the early phase, gravitational waves associated with inspiral motion are seen. After the onset of tidal disruption, the amplitude quickly damps, and eventually, waveforms are characterized by a ringdown oscillation of small amplitude associated with a quasinormal mode of the BH. This qualitative agreement confirms the conclusion about gravitational waveforms in the previous paper [30].

Figure 20(d) plots angular velocity of gravitational waves for runs BHNS-B1–B3 and BHNS-A1. For BHNS-A1, the curve is plotted as a function of $t_{\rm ret} + 266M_0$. The dotted curve denotes the result predicted by the Taylor T4 formalism for $m_0\Omega_0 = 0.034$ and 0.036. This also shows that the binary for model BHNS-B is in an eccentric orbit, because Ω considerably modulates with time. The plots for runs BHNS-B1–B3 clarify again that the value of $T_{\rm disr}$ depends strongly on the grid resolution. The results for runs BHNS-A1 and BHNS-B1 agree approximately for the late inspiral phase. This is expected because the waveforms for both models are similar as shown in Figs. 20(a) and 20(b). The curve for run BHNS-B1 does not agree with that derived by the Taylor T4 formalism for $m_0\Omega_0 = 0.034$, but agree relatively with that for $m_0\Omega_0 = 0.036$. Part of the reason is that the inspiral time is spuriously shortened by numerical dissipation. Another possible reason is that the binary has a large eccentricity initially, which enhances gravitational wave emission and shortens the inspiral time; namely, an averaged orbital velocity of the initial condition does not satisfy $m_0\Omega_0 = 0.034$ but may be close to $m_0\Omega_0 = 0.036$.

V. SUMMARY

We have reported our new numerical relativity code, named SACRA, in which an AMR algorithm is imple-

mented. In this code, the Einstein evolution equations are solved in the BSSN formalisms with a fourth-order spatial finite-differencing scheme, the hydrodynamic equations are solved by a third-order high-resolution central scheme, and the time integration is done in the fourth-order Runge-Kutta scheme. Both F_i-type and $\tilde{\Gamma}^i$-type BSSN formalisms are implemented. In both cases, $W = e^{-2\phi}$ is evolved instead of evolving ϕ. This enables us to adopt grid-center-grid coordinates.

A. Technical points and issues for the future

To check the feasibility of SACRA, we performed simulations for coalescence of BH-BH, NS-NS, and BH-NS binaries. All the simulations were performed on personal computers using at most 5 GBytes of memory. The required CPU time is at most 1 month even for the best-resolved runs. For simulating BH-BH binaries, we employed the same initial conditions as those adopted by Buonanno *et al.* [23]. Our results agree with theirs in a reasonable manner except for a slight disagreement possibly associated with the difference in choices of gauge conditions and numerical scheme. We also show that our code can follow inspiraling BH-BH binaries at least for about 4.5 orbits even in the absence of dissipation term such as the Kreiss-Oliger-type dissipation term. This implies that even in the AMR code, the dissipation term is not always necessary, if appropriate schemes for interpolation and extrapolation are employed for the procedures at refinement boundaries.

Our numerical results for BH-BH binaries indicate that for accurately evolving final 2.5 orbits before the merger, a relatively small number of grid points is sufficient. The orbit of the BH is computed accurately and, as a result, gravitational waveforms are computed with a small phase error. In the present simulations, the used memory is at most 3 GBytes, and a personal computer with 4 GBytes of memory is sufficient for accurate evolution of the final phase of BH-BH binaries.

By contrast, numerical results, in particular, the merger time, depend strongly on the grid resolution, grid structure, and gauge condition for evolving ≈ 4.5 inspiral orbits. The estimated phase error in gravitational waveforms for such cases is about $40m_0$ even in the finest-resolution simulation in this paper. For obtaining convergent results within the phase error of, say, $10m_0$ for the entire evolution, the grid resolution has to be finer by a factor of ~ 2. However, we note the following: Numerical results for the final state of the BH formed after merger do not depend on the grid resolution as strongly as the merger time and gravitational wave phase. It should be noted that for determining the final state of the BH within a 1% error, it is not necessary to take a high-grid resolution. We find that the present choice is appropriate.

We find that the merger time and gravitational wave phase could depend on spatial gauge conditions. The reason for this is explained as follows: The physical grid spacing and grid structure depend on the spatial gauge condition, in particular, around BHs. Thus, the magnitude of numerical dissipation also depends on the spatial gauge and may be reduced for a simulation performed with an appropriate choice for the spatial gauge, even if the same grid structure is employed. Therefore, an appropriate choice of the spatial gauge condition may reduce computational costs, and a careful choice is required.

We also show that our code can evolve NS-NS and BH-NS binaries. Numerical results obtained by SACRA agree with those in the previous simulations, if we resolve the NSs and BHs by approximately the same accuracy. However, the computational cost is at most 5% of the previous unigrid simulations, and the robustness of the AMR scheme is confirmed. Simulations with much better accuracy than those in the previous simulations can be performed by less computational costs. Because we performed the simulations for a wide range of grid resolutions, we can also estimate the magnitude of the phase error of gravitational waveforms in the present and previous numerical results [30] in an inexpensive computational cost.

We followed the inspiral phase of BH-NS binaries for a long time (~ 4 orbits) for the first time. In the best-resolved simulation, the inspiral orbit up to the onset of tidal disruption is followed for about 3.7 orbits. Subsequent merger and ringdown phases are also computed well for producing gravitational waveforms. However, we find that the prepared quasicircular initial condition has a large eccentricity, and the inspiral orbit is highly eccentric for the first ~ 2 orbits, although the eccentricity for a few orbits just before the merger is reduced by the emission of gravitational waves. To perform a realistic simulation for the inspiral phase with small eccentricity, it is necessary to improve the initial condition (see, e.g., Ref. [62] for a method). This is an issue for the future.

We compare the duration spent in the inspiral phase obtained by numerical simulations with that predicted by the Taylor T4 formalism for BH-BH and BH-NS binaries. For long-term runs with the merger time $\gtrsim 500M_0$, the merger time determined by extrapolation of the numerical results agree with the prediction by the Taylor T4 formalism within an error of $\sim 10\%$. This makes us reconfirm that the Taylor T4 formalism provides a good semi-analytical estimate for the time spent in the inspiral phase. We also find that the Taylor T4 formalism always provides an overestimated value of the merger time for NS-NS and BH-NS binaries. The reason for this overestimation is that in this formalism, tidal effects of NSs, which accelerate the infalling process to merger, are not included. Nevertheless, the error is not extremely large, because tidal effects play a crucial role only for close orbits. Therefore, for validating a numerical result, it is useful to compare the merger time with the result derived by the Taylor T4 formalism.

We find that the convergence of the merger time for NS-NS binaries is relatively slow. For this case, the evolution

of NSs in the late inspiral phase depends on the effects of tidal deformation of each NS, which in general shortens the merger time. Thus, to accurately determine the orbital evolution, the tidal deformation of each NS has to be followed accurately in hydrodynamics. The degree of tidal deformation is in general larger near the surface of the NS, because the tidal force is approximately proportional to the distance from the center of each NS. In our AMR scheme, the grid resolution around the surface region is not as high as that in the central region. Consequently, the tidal deformation is not followed as accurately as that in the central region. A simple way to overcome this problem is to resolve the surface region as accurately as the central region, i.e., to cover each NS in the finest level. However, doing this in our present scheme is computationally expensive, because we have to choose a large value of N for the finest level. There may be a better grid structure to overcome this problem, e.g., to change the cube size in each refinement level. Improving our AMR scheme is an issue in the next step. A completely alternative possibility is to employ a different hydrodynamic scheme that is less dissipative. Improving this scheme is also an issue in the future.

We note that the final state of the BH and surrounding disk after merger of NS-NS binaries do not depend on the grid resolution as strongly as the merger time. This property is the same as that in the case of BH-BH binaries. Thus, for studying the final state, the present choice of the grid resolution is acceptable.

We check whether or not the conservation relations of energy and angular momentum denoted by Eqs. (67) and (68) or by Eqs. (69) and (70) hold. The energy conservation holds within $\sim 1\%$ error irrespective of the binary components for the best-resolved run. The error of angular momentum conservation is larger: The error is $\sim 3\%$–5%. The resulting total energy and angular momentum of BHs are always smaller than the values predicted by the conservation relations, and hence, numerical dissipation is the most likely source of the error. The error size for the angular momentum conservation may not be negligible, in particular, for studying disk formation around the BH formed after merger. In our results, the disk mass is likely to be underestimated. Indeed, the result for the disk mass in this paper does not agree with the previous result of a BH-NS binary [30]. In the previous result, the angular momentum conservation holds in a much better manner. Thus, the small disk mass in the present results might be partly due to the spurious loss of angular momentum [63].

Another possible drawback in our present AMR scheme is that we might not be able to accurately follow material that spreads around the BH after tidal disruption of the NS. The reason is that a large fraction of material escapes from the finest level soon after the onset of tidal disruption. The motion of such material orbiting the BH is located at relatively coarser levels and hence it may not be followed accurately. The material, which forms a spiral arm around the BH, subsequently falls into the BH in a short time scale in the present result. This may be in part due to the fact that its angular momentum is spuriously dissipated. In the present simulations, we found that the resulting mass of accretion disk is much smaller than $10^{-3}M_*$ for $q \approx 0.33$ and $M_{\rm NS}/R_{\rm NS} = 0.145$. This result totally disagrees with our previous results [30,60] as mentioned above. Note that the evolution of binaries up to tidal disruption agrees well indicating that the grid structure is appropriate at least up to the onset of tidal disruption. This suggests that the grid structure in our AMR code might not be well suited only for following the material orbiting the BH of a distant orbital separation. To improve this situation, it may be necessary to prepare a fine grid that covers a larger region around the BH. To perform such a simulation, it will be necessary to change the grid structure, e.g., to increase the grid number for the finer levels while fixing that for the coarser levels. Such improvement of our current AMR scheme is an issue in the next step.

B. Comparison of numerical results for three types of binaries

We performed simulations for three types of binaries. Because of the presence of strong equivalence principle, the orbital evolution and gravitational waveforms in the inspiral phase with a large orbital separation depend very weakly on the components of the binaries. By contrast, the final outcome and gravitational waveforms in the merger phase depend strongly on the components. As already found in the previous studies (e.g., [23]), we found that after merger of slowly spinning two equal-mass BHs, a rotating BH with spin ≈ 0.7 is formed. However, the magnitude of the spin parameter is much higher for a BH formed after merger of NS-NS binaries: The present results show that the spin is ~ 0.8–0.85. This disagreement comes primarily from the difference in amplitude of gravitational waves emitted in the final merger phase. In the case of BH-BH binaries, the BHs can have a closer orbit than the NSs, because the BHs are more compact. As a result, gravitational waves are significantly emitted in the final inspiral orbit. In addition, the quasinormal mode oscillation of fundamental $l = m = 2$ mode is excited significantly in the merger phase. Indeed, the gravitational wave amplitude is as high as that emitted at the last inspiral orbit (cf. Figure 4). By these gravitational wave emissions, the angular momentum is significantly dissipated in the final phase. By contrast, in the case of NS-NS binaries, the merger sets in at a relatively distant orbit, because NSs are not as compact as BHs, and moreover, the quasinormal mode is not excited as significantly as in the case of BH-BH binaries because of smaller degree of nonaxisymmetric deformation of the spacetime curvature at the merger.

Because of the difference in amplitude of ringdown gravitational waveforms, the property of gravitational

waveforms in the final merger phase depends strongly on the binary components. As mentioned above, the amplitude of ringdown gravitational waves is as high as that in the last inspiral phase for the merger of BH-BH binaries. By contrast, the amplitude is ~10% as high as that in the last inspiral phase for the merger of NS-NS binaries. Thus, the wave amplitude quickly decreases in this case.

We also study the merger of BH-NS binaries. In the present paper, we focus on the case that the NS is tidally disrupted before it is swallowed by the companion BH. In this case, the quasinormal mode is not significantly excited as in the case of NS-NS binaries, and hence, the amplitude of ringdown gravitational waves is also much smaller than that in the last inspiral orbit. However, this may not be always the case. If the mass ratio $q(= M_{\rm NS}/M_{\rm BH})$ is small enough, the NS will not be tidally disrupted before swallowing by the BH. In such case, a quasinormal mode may be excited significantly at a moment that the NS falls into the BH. This topic should be investigated in future work.

As summarized in this section, gravitational waveforms at merger phase depend strongly on the binary components. This makes us reconfirm that gravitational waves at merger phase will carry information about the properties of binary components. As reviewed in Sec. I, a number of simulations have been performed in the past decade. However, there are huge parameter spaces for which numerical study has not been done yet, in particular, for NS-NS and BH-NS binaries. Obviously, further study is required. Our new code SACRA will be able to make a contribution to this purpose.

ACKNOWLEDGMENTS

We thank L. Baiotti and Y. Sekiguchi for helpful discussions, and K. Kyutoku and H. Okawa for their help. We also would like to thank H. Pfeiffer and his collaborators for providing initial data of BH-BH binaries for open use (see Ref. [44]). Numerical computations were in part performed on the NEC-SX8 at Yukawa Institute of Theoretical Physics of Kyoto University. This work was supported by Monbukagakusho Grant No. 19540263.

APPENDIX A: APPARENT HORIZON FINDER

Apparent horizon is defined as a marginally outermost trapped two surface on which the following equation is satisfied:

$$K - K_{ij}s^i s^j - D_i s^i = 0. \tag{A1}$$

Here, s^i denotes a unit normal vector, orthogonal to the two surface of the apparent horizon. Denoting the location of the apparent horizon as $r = h(\theta, \varphi)$ for an appropriately chosen coordinate center, s_i is written as

$$s_i = CW^{-1}(1, -h_{,\theta}, -h_{,\varphi}), \tag{A2}$$

where $C = (\tilde{\gamma}^{ij}s_i s_j)^{-1/2}$. Substituting Eq. (A2) into Eq. (A1), the equation for $h(\theta, \varphi)$ is derived, and its schematic form is

$$h_{,\theta\theta} + \cot\theta h_{,\theta} + \frac{h_{,\varphi\varphi}}{\sin^2\theta} - 2h = S, \tag{A3}$$

where S denotes the source term composed of γ_{ij}, K_{ij}, h, and its derivatives. In the method of Ref. [40], we write the source term in a straightforward manner and solve the 2D elliptic-type Eq. (A3) iteratively.

In SACRA, first of all, we slightly change the form of the basic equation, simply rewriting Eq. (A1) as

$$\begin{aligned} h_{,\theta\theta} + \cot\theta h_{,\theta} + \frac{h_{,\varphi\varphi}}{\sin^2\theta} - 2h \\ = h_{,\theta\theta} + \cot\theta h_{,\theta} + \frac{h_{,\varphi\varphi}}{\sin^2\theta} - 2h \\ - (K - K_{ij}s^i s^j - D_i s^i)/(CW), \end{aligned} \tag{A4}$$

where on the right-hand side, we input trial values for h in each iteration step. In our previous method, $D_i s^i$ is calculated to be a complicated function of h, $h_{,\theta}$, $h_{,\theta\theta}$, $h_{,\varphi}$, $h_{,\varphi\varphi}$, $h_{,\theta\varphi}$, and γ^{ij}. In the present method, we simply use a finite differencing for evaluating $D_i s^i$. Namely, we write it as

$$\begin{aligned} W^3\Bigg[\frac{1}{r^2}\partial_r(r^2 W^{-3}s^r) + \frac{1}{\sin\theta}\partial_\theta(\sin\theta W^{-3}s^\theta) \\ + \partial_\varphi(W^{-3}s^\varphi)\Bigg], \end{aligned} \tag{A5}$$

and evaluate each term by the second-order finite-differencing. Here, ∂_θ and ∂_φ are evaluated on the apparent horizon and hence the evaluation is straightforward, whereas ∂_r cannot be evaluated on the apparent horizon. To compute it, we prepare two dummy points for each point of (θ, φ), which are located at slightly outside and inside of the apparent horizon along an orthogonal direction with respect to the two surface. The coordinate distance from those dummy points to the apparent horizon is chosen to be $\approx h/20$. By this method, the source term of Eq. (A4) is significantly simplified.

With this setting, the solution of h is obtained by solving 2D elliptic-type Eq. (A4). The method for solving this equation is the same as that described in detail in Ref. [40]. We compare the results of the apparent horizon mass obtained in the present and previous methods and find that both results agree well.

APPENDIX B: NUMERICAL RESULTS FOR BH-BH BINARY WITH A DIFFERENT INITIAL CONDITION OF GAUGE VARIABLES

As we mentioned in Sec. IVA, the coordinate trajectory of BHs in inspiraling BH-BH binaries depends strongly on the initial condition for β^k, although gravitational waveforms depend only very weakly on it. This appendix is denoted to a summary of the results. Specifically, we performed two simulations for $d = 19$ using the solution

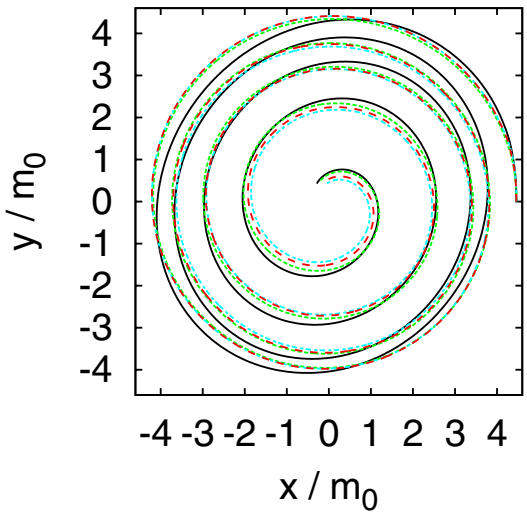

FIG. 21 (color online). The same as Fig. 1, but for runs 19a'(solid curve) and 19aF' (dashed curve). The trajectories for runs 19a and 19aF are shown together by the dotted and dotted-dashed curves.

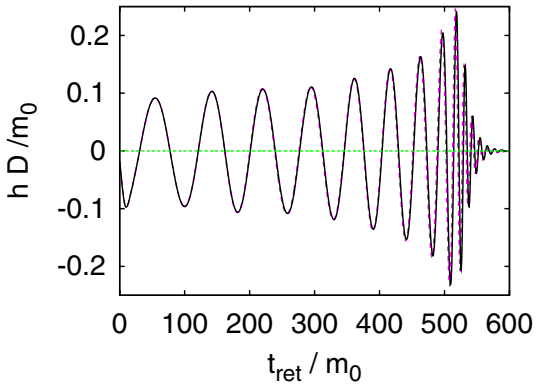

FIG. 22 (color online). Gravitational waveforms (plus mode) for runs 19a (dashed curve) and 19a'(solid curve), respectively.

TABLE X. The same as Table III, but for runs 19a' and 19aF'.

Run	$T_{\rm AH}/m_0$	$M_{\rm irr}/m_0$	C_p/C_e	$C_e/(4\pi m_0)$	$M_{\rm BHf}/m_0$	a	$\Delta E/m_0$	$\Delta J/J_0$	Level
19a'	518.5	0.879	0.891	0.949	0.950	0.702	0.035	0.28	$L-1$
19aF'	507.3	0.879	0.891	0.949	0.950	0.702	0.035	0.28	$L-1$

of the quasi-equilibrium condition for the gauge variables as the initial condition. We prepared the same grid structure as that of runs 19a and 19aF. The simulations were performed both in the $\tilde{\Gamma}^i$- and F_i-BSSN formalisms. Hereafter these simulations are referred to as runs 19a' and 19aF', respectively.

Figure 21 plots the coordinate trajectories for runs 19a' and 19aF' together with those for runs 19a and 19aF. We find that for run 19a', the trajectory is highly elliptical and different from that of run 19a. By contrast, the trajectory of run 19aF' is approximately the same as that of run 19aF. For runs 19a' and 19aF', the merger time is slightly longer than that for runs 19a and 19aF. However, the parameters of BHs finally formed depend very weakly on the initial condition for the gauge variables (see Table X).

Although the coordinate trajectory depends on the initial condition for gauge variables, this is purely a gauge effect. One evidence is found from the fact that the merger time for runs 19a and 19a' is approximately the same (see Table X). To further show the evidence for this, we generate Fig. 22, which compares the gravitational waveforms of runs 19a and 19a'. This figure shows that two waveforms agree approximately with each other besides a small phase error in the final phase. This indicates that the waveform for run 19a' is not as elliptic as the trajectory suggests, and hence, the orbit is physically circular.

[1] Buonanno *et al.* Phys. Rev. D **75**, 124018 (2007).
[2] L. Blanchet, Living Rev. Relativity **9**, 4 (2006).
[3] M. Shibata and K. Uryū, Phys. Rev. D **61**, 064001 (2000); Prog. Theor. Phys. **107**, 265 (2002).
[4] M. Shibata, K. Taniguchi, and K. Uryū, Phys. Rev. D **68**, 084020 (2003); **71**, 084021 (2005); M. Shibata and K. Taniguchi, *ibid.* **73**, 064027 (2006).
[5] M. D. Duez, P. Marronetti, S. L. Shapiro, and T. W. Baumgarte, Phys. Rev. D **67**, 024004 (2003).
[6] M. Miller, P. Gressman, and W.-M. Suen, Phys. Rev. D **69**, 064026 (2004).
[7] Y.-T. Liu, S. L. Shapiro, Z. B. Etienne, and K. Taniguchi, arXiv:0803.4193.
[8] L. Baiotti, B. Giacomazzo, and L. Rezzolla, arXiv:0804.0594.
[9] M. Anderson, E. W. Hirschmann, L. Lehner, S. L. Liebling, P. M. Motl, D. Neilsen, C. Palenzuela, and J. E. Tohline, Phys. Rev. D **77**, 024006 (2008); Phys. Rev. Lett.

100, 191101 (2008).
[10] J. Read, J. Creighton, J. L. Friedman, C. Markakis, M. Shibata, and K. Uryū (unpublished).
[11] K. Kiuchi, Y. Sekiguchi, M. Shibata, and K. Taniguchi (unpublished).
[12] F. Pretorius, Phys. Rev. Lett. **95**, 121101 (2005); Classical Quantum Gravity **23**, S529 (2006).
[13] M. Campanelli, C. O. Lousto, P. Marronetti, and Y. Zlochower, Phys. Rev. Lett. **96**, 111101 (2006); M. Campanelli, C. O. Lousto, Y. Zlochower, and D. Merritt, Phys. Rev. Lett. **98**, 231102 (2007); M. Campanelli, C. O. Lousto, and Y. Zlochower, Phys. Rev. D **73**, 061501(R) (2006); **74**, 041501 (2006); **74**, 084023 (2006).
[14] J. G. Baker, J. Centrella, D.-I. Choi, M. Koppitz, and J. van Meter, Phys. Rev. Lett. **96**, 111102 (2006); Phys. Rev. D **73**, 104002 (2006); J. G. Baker, J. Centrella, D.-I. Choi, M. Koppitz, J. van Meter, and M. C. Miller, Astrophys. J. **653**, L93 (2006).
[15] P. Diener, F. Herrmann, D. Pollney, E. Schnetter, E. Seidel, R. Takahashi, J. Thornburg, and J. Ventrella, Phys. Rev. Lett. **96**, 121101 (2006); D. Pollney, C. Reisswig, L. Rezzolla, B. Szilagyi, M. Ansorg, B. Deris, P. Diener, E. N. Dorband, M. Koppitz, A. Nagar, and E. Schnetter, Phys. Rev. D, **76**, 124002 (2007); M. Koppitz, D. Pollney, C. Reisswig, L. Rezzolla, J. Thornburg, P. Diener, and E. Schnetter, Phys. Rev. Lett. **99**, 041102 (2007); L. Rezzolla, P. Diener, E. N. Dorband, D. Pollney, C. Reisswig, E. Schnetter, and J. Seiler, Astrophys. J. **674**, L29 (2008);L. Rezzolla, E. N. Dorband, C. Reisswig, P. Diener, D. Pollney, E. Schnetter, and B. Szilagyi Astrophys. J. **679**, 1422 (2008).
[16] M. A. Scheel, H. P. Pfeiffer, L. Lindblom, L. E. Kidder, O. Rinne, and S. A. Teukolsky, Phys. Rev. D **74**, 104006 (2006).
[17] B. Brügmann, J. A. Gonzalez, M. Hannam, S. Husa, U. Sperhake, and W. Tichy, Phys. Rev. D **77**, 024027 (2008).
[18] B. Szilágyi, D. Pollney, L. Rezzolla, J. Thornburg, and J. Winicour, Classical Quantum Gravity **24**, S275 (2007).
[19] J. G. Baker, M. Campanelli, F. Pretorius, and Y. Zlochower, Class. Quantum Grav. **24**, S25 (2007).
[20] L. Herrmann, I. Hinder, D. Shoemaker, P. Laguna, and R. A. Matzner, Astrophys. J. **661**, 430 (2007).
[21] C. F. Sopuerta, N. Yunes, and P. Laguna, Astrophys. J. **656**, L9 (2007).
[22] J. A. Gonzalez, U. Sperhake, B. Brügmann, M. Hannam, and S. Husa, Phys. Rev. Lett. **98**, 091101 (2007); J. A. Gonzalez, M. Hannam, U. Sperhake, B. Brügmann, and S. Husa, Phys. Rev. Lett. **98**, 231101 (2007).
[23] A. Buonanno, G. B. Cook, and F. Pretorius, Phys. Rev. D **75**, 124018 (2007).
[24] J. G. Baker, S. T. McWilliams, J. R. van Meter, J. Centrella, D.-I. Choi, B. J. Kelly, and M. Koppitz, Phys. Rev. D **75**, 124024 (2007).
[25] H. P. Pfeiffer, D. A. Brown, L. E. Kidder, L. Lindblom, G. Lovelace, and M. A. Scheel, Class. Quantum Grav. **24**, S59 (2007).
[26] M. Hannam, S. Husa, U. Sperhake, B. Brügmann, and J. A. González, Phys. Rev. D **77**, 044020 (2008).
[27] P. Marronetti, W. Tichy, B. Brügmann, J. A. González, and U. Sperhake, Phys. Rev. D **77**, 064010 (2008).
[28] M. Boyle, D. A. Brown, L. E. Kidder, A. H. Mroue, H. P. Pfeiffer, M. A. Scheel, G. B. Cook, and S. A. Teukolsky, Phys. Rev. D **76**, 124038 (2007); M. Boyle *et al.*, arXiv:0804.4184.
[29] M. Shibata and K. Uryū, Phys. Rev. D **74**, 121503(R) (2006); Class. Quantum Grav. **24**, S125 (2007).
[30] M. Shibata and K. Taniguchi, Phys. Rev. D **77**, 084015 (2008).
[31] Z. B. Etienne, J. A. Faber, Y. T. Liu, S. L. Shapiro, K. Taniguchi, and T. W. Baumgarte, Phys. Rev. D. **77**, 084002 (2008).
[32] A. Akmal, V. R. Pandharipande, and D. G. Ravenhall, Phys. Rev. C **58**, 1804 (1998).
[33] M. Shibata, Phys. Rev. Lett. **94**, 201101 (2005).
[34] M. Berger and J. Oliger, J. Comp. Physiol. **53**, 484 (1984).
[35] SACRA is named after Sakura in Japanese (cherry blossom in English).
[36] A. Kurganov and E. Tadmor, J. Comput. Phys. **160**, 241 (2000).
[37] M. Shibata and T. Nakamura, Phys. Rev. D **52**, 5428 (1995); T. W. Baumgarte and S. L. Shapiro, Phys. Rev. D **59**, 024007 (1998).
[38] M. Alcubierre, B. Brügmann, P. Diener, M. Koppitz, D. Pollney, E. Seidel, and R. Takahashi, Phys. Rev. D **67**, 084023 (2003).
[39] M. Shibata and J. A. Font, Phys. Rev. D **72**, 047501 (2005).
[40] M. Shibata, Phys. Rev. D **55**, 2002 (1997); M. Shibata and K. Uryū, Phys. Rev. D **62**, 087501 (2000).
[41] G. B. Cook and H. P. Pfeiffer, Phys. Rev. D **70**, 104016 (2004).
[42] H. P. Pfeiffer, L. E. Kidder, M. A. Scheel, and S. A. Teukolsky, Comput. Phys. Commun. **152**, 253 (2003).
[43] M. Caudill, G. B. Cook, J. D. Grigsby, and H. P. Pfeiffer, Phys. Rev. D **74**, 064011 (2006).
[44] http://www.black-holes.org/researchers3.html/
[45] D. Brown *et al.*, Phys. Rev. D **76**, 081503(R) (2007).
[46] Z. B. Etienne, J. A. Faber, Y. T. Liu, S. L. Shapiro, and T. W. Baumgarte, Phys. Rev. D **76**, 101503(R) (2007).
[47] E. W. Leaver, Proc. R. Soc. A **402**, 285 (1985); F. Echeverria, Phys. Rev. D **40**, 3194 (1989).
[48] J. R. Wilson and G. J. Mathews, Phys. Rev. Lett. **75**, 4161 (1995).
[49] C. S. Kochanek, Astrophys. J. **398**, 234 (1992); L. Bildsten and C. Cutler, *ibid.* **400**, 175 (1992).
[50] E. Gourgoulhon, P. Grandclément, K. Taniguchi, J.-A. Marck, and S. Bonazzola, Phys. Rev. D **63**, 064029 (2001).
[51] K. Taniguchi and E. Gourgoulhon, Phys. Rev. D **66**, 104019 (2002); **68**, 124025 (2003).
[52] LORENE website: http://www.lorene.obspm.fr/.
[53] K. Uryū, M. Shibata, and Y. Eriguchi, Phys. Rev. D **62**, 104015 (2000).
[54] D. Lai, F. A. Rasio, and S. L. Shapiro, Astrophys. J. Suppl. Ser. **88**, 205 (1993).
[55] E. Berti, S. Iyer, and C. M. Will, Phys. Rev. D **77**, 024019 (2008).
[56] P. Grandclément, Phys. Rev. D **74**, 124002 (2006); **75**, 129903(E) (2007).
[57] K. Taniguchi, T. W. Baumgarte, J. A. Faber, and S. L. Shapiro, Phys. Rev. D **75**, 084005 (2007).
[58] K. Taniguchi, T. W. Baumgarte, J. A. Faber, and S. L.

Shapiro, Phys. Rev. D **77**, 044003 (2008).
[59] K. Kyutoku, M. Shibata, and K. Taniguchi (unpublished).
[60] Although disk mass is very small in the present numerical results for $M_{\rm NS}/M_{\rm BH} \approx 0.33$ and $M_{\rm NS}/R_{\rm NS} \approx 0.145$, this does not imply that the disk mass is always negligible irrespective of the mass ratio and compactness of NS. Indeed, for a large value of $M_{\rm NS}/M_{\rm BH}$ as $1/2$, disk of mass $\sim 0.01 M_{\rm NS}$ is formed for $M_{\rm NS}/R_{\rm NS} \approx 0.145$ in our latest numerical results obtained by SACRA (unpublished work in progress). Thus, we here mention that the dependence of the disk mass on the mass ratio and compactness of NS for the results derived by SACRA does not agree with the previous one reported in Ref. [30].
[61] P. J. Montero, J. A. Font, and M. Shibata, arXiv:0805.3099 [Phys. Rev. D (to be published)].
[62] F. Foucart, L. E. Kidder, H. P. Pfeiffer, and S. A. Teukolsky, arXiv:0804.3787.
[63] However, it is also possible that the previous result on the disk mass might be rather inaccurate and better conservation of angular momentum might be purely by chance. Also, worth noting is that viscosity-induced dissipation does not change total angular momentum. Thus, it is possible that viscosity associated with numerical error in the previous simulation might be rather large.